Performance Investigation on Elevation Cascaded Digital Beamforming for Multidimensional Waveform Encoding SAR Imaging

HE Feng* ZHANG Yongsheng SUN Zaoyu JIN Guanghu DONG Zhen*

(*College of Electronic Science and Technology, National University of Defense Technology, Changsha* 410073, *China*)

Abstract: An important issue in a Synthetic Aperture Radar (SAR) system employing Multidimensional Waveform Encoding (MWE) is the fulfillments of Digital BeamForming (DBF) on receive in elevation for a reliable separation of the mutually overlapped echoes from multiple transmit waveforms. In this paper, the performance of a separation approach employing hybrid DBF in elevation by combining the onboard real-time beamsteering and a posteriori null-steering DBF on the ground is elaborately investigated. As a cascaded structure which comprises two subsequent DBF networks, the onboard part effectuates the steering of the mainlobes within multiple partitioned groups of antenna elements to ensure sufficient signal receive gain over the whole swath; the a posteriori adaptive DBF network on the ground mainly performs the task of placing nulls to cancel the range interference from other transmit waveforms, which enables adaptive beamforming to avoid the topographic height variation problem. Two type of onboard realtime beamformers are investigated, depending on the utilization of the transmit waveform structure information or not. The performance of the hybrid DBF approach is theoretically analyzed and evaluated in simulation experiment. It is shown that the hybrid DBF approach can provide additional dimensions of the trade-space to optimize the performance on range ambiguity suppression and signal-to-noise ratio improvement, as well as the onboard data volume reduction. In comparison with the a posteriori DBF on the ground, employing the hybrid DBF networks can get satisfactory performance while remarkably reducing the output data volume, in the presented example, the corresponding output channel number is decreased from 10 to 6.

Key words: Digital BeamForming (DBF); Multidimensional Waveform Encoding (MWE); Multiple-Input Multiple-Output (MIMO); Synthetic Aperture Radar (SAR); Range ambiguity

DOI: 10.12000/JR20107

Reference format: HE Feng, ZHANG Yongsheng, SUN Zaoyu, *et al*. Performance investigation on elevation cascaded digital beamforming for multidimensional waveform encoding SAR imaging[J]. *Journal of Radars*, 2020, 9(5): 828–855. DOI: 10.12000/JR20107.

引用格式：何峰, 张永胜, 孙造宇, 等. 多维波形编码SAR俯仰向级联DBF成像性能分析[J]. 雷达学报, 2020, 9(5): 828–855. DOI: 10.12000/JR20107.

多维波形编码SAR俯仰向级联DBF成像性能分析

何 峰* 张永胜 孙造宇 金光虎 董 臻*

(国防科技大学电子科学学院 长沙 410073)

摘 要：在采用多维波形编码(MWE)技术的新体制合成孔径雷达(SAR)系统中，利用俯仰向的数字波束形成(DBF)来实现多个发射波形重叠回波的可靠分离是一个关键问题。该文详细研究了星上实时波束控制与地面后置零陷控制相结合的混合俯仰向DBF分离方法的成像性能问题。 作为一种包括星地两级DBF网络的级联结构，其中的星上部分通过在划分的多个天线子孔径上实现实时主瓣波束指向控制，确保在整个测绘上足够的信号接收增益; 而后置自适应DBF网络主要完成零陷抑制的任务，以消除其它发射波形带来的距离向干扰，可自适应于地形高度起伏变化带来的视角变化。根据对发射波形时频结构先验信息的利用情况，提出了两种星上实时波束形成器

Manuscript received July 23, 2020; Revised September 28, 2020; Published online October 16, 2020.

*Communication author: HE Feng; DONG Zhen

E-mail: hefeng@nudt.edu.cn; dongzhen@nudt.edu.cn

Foundation Item: The National Natural Science Foundation of China (61771478)

Corresponding Editor: WANG Yanfei

的实现方式。对混合DBF方法下的成像信噪比和模糊度性能进行了理论建模与仿真实验评估。实验结果表明，混合DBF方法可以为优化图像模糊度和信噪比性能提供额外的设计自由度，并降低星上数据通道数目。与纯地面DBF网络相比，采用混合DBF网络可以在显著减少星上输出数据量的同时获得满意的性能，在给出的实例中，实现相近性能的条件下，相应的星上数据通道数从10个减少到6个。

关键词：数字波束形成；多维波形编码；多发多收；合成孔径雷达；距离模糊
中图分类号：TN929.5 **文献标识码**：A **文章编号**：2095-283X(2020)05-0828-28

1 Introduction

Synthetic Aperture Radar (SAR) is a well-proven imaging technique for remote sensing[1]. However, conventional spaceborne SAR systems are not capable of fulfilling the increasing demands for improved spatial resolution and wider swath coverage, due to the inherent limitation imposed by range and azimuth ambiguities[1–3]. This motivated the development of new radar techniques to overcome the classical limitation. A promising technique among them is Digital Beam-Forming (DBF) on receive[2,3], where the receive antenna is split into multiple subapertures in azimuth direction. The additional information filled in the data space collected by these receive apertures will be used to reconstruct unambiguous SAR signal without a reduction of the imaged area.

As a natural and important complement to DBF on receive, the innovative concept of Multi-dimensional Waveform Encoding (MWE) on transmit was advocated[4–11]. MWE is a new digital beamforming technique on transmit utilizing multiple transmitters, which is closely tied up with the concept of Multiple-Input–Multiple-Output (MIMO) SAR[9–17]. In combination with 2-dimensional DBF on receive with multiple receivers, a multi-transmit and multi-receive architecture, also known as MIMO, is formed which employs a novel fully active DBF technique utilizing the full area of the same antenna aperture for both transmission and reception with a wide scene illumination[4,11].

One of the innovative characteristics of the multichannel receiver in MWE-SAR system is that besides the Degrees Of Freedom (DOF) provided by multiple channels in azimuth dimension, there are also additional DOFs provided by multiple elevation channels[11]. The additional DOFs in elevation then can be exploited with the MWE technique to realize waveform diversity in space-time domain and collecting more new information about the object space. Therefore, MWE SARs are promising for HRWS imaging or even fully polarimetric SAR with HRWS imaging ability[4,11–16,18]. Another major benefit of multiple subapertures in elevation is the ability to increase the receive power, like the case of DBF-SAR system[19–22].

An important issue in a MWE-SAR system is the fulfillment of DBF on receive in elevation for a reliable separation of the mutually overlapped echoes from different transmit waveforms, according to their different Directions Of Arrival (DOA)[5–12] at the same arrival instant. In Ref. [6,7], a new separation approach for MWE SAR was suggested, implemented by an onboard Advanced Null-Steering (ANS) beamformer. By using the multi-channel data collected by all antenna elements/subapertures from the full antenna area in elevation dimension, multiple real-time narrow receive beams with well-designed nulls are formed in parallel on the satellite. Each receive beam is responsible to separate one of the transmit waveform echo: it not only tracks echo from one transmit waveform as it travels on the ground by directing the high-gain beam to the varying direction of the echo arrival, but also totally rejects interferences from other directions corresponding to the rest of transmit waveform echoes by time-varying null steering. In the best scenario, the onboard ANS beamformer could achieve the goal of echo separation satisfactorily: it receives echo from one transmit waveform with high receive gain due to the full receive aperture in elevation (in analogy to the onboard DBF process called scanning on receive, *i.e.* SCORE[21,22] for a DBF-SAR system), as well as deeply sup-

presses echoes from all other transmit waveforms. In the meantime, the huge data volume before beamforming, which is multiplied by the large number of receive elements/channels in elevation, is maximally reduced[7]: the output channel number in elevation after the onboard real-time DBF is only the number of transmit waveforms. However, due to the limited digital resources onboard the satellite, the real-time beamformer is normally a deterministic one (non-adaptive beam/null steering) for the non-range-compressed raw data and the expected ideal performance could be largely deteriorated.

The principle problem of this full real-time deterministic DBF process is caused by the variation of topographic height[4]. The time-varying steering angle is normally pre-determined using a simplified Earth geometric model, *e.g.* an ellipsoid Earth model[4,6,7], or further modified according to the local average topographic height. However, under model-mismatch conditions in presence of topographic height variations, erroneous steering of the full-aperture focused sharp main beam and deep nulls will result in a reduced signal gain and insufficient interference suppression[4]. The insufficiently suppressed interference will introduce residual range ambiguities in SAR image. On the whole, it means a deterioration of system performance on SNR (signal-to-noise ratio) and Range Ambiguity-to-Signal Ratio (RASR), which can greatly affect the quality of the achieved SAR images. Since the antenna pattern near null is rather steep, the loss on interference suppression will be much more severe and may be unacceptable[8]. Improved onboard adaptive beam/null steering approaches are suggested for MWE-SAR or DBF-SAR systems[5,23], but they will hugely increase digital resources for spaceborne SAR.

Another concern on the real-time ANS-beamformer is the Pulse Extension Loss (PEL) effect[20,21]. The ground area contributing to the echo at any instance of time is referred to as the pulse extent[21], it depends on the pulse duration and travels predictably on the ground under a given geometry. However, the time-varying beam and nulls are normally precisely designed to point to the center of pulse extent of the transmit waveforms at a given time. Since ANS-beamformer uses all the channels in elevation to form a sharp high-gain receive beam, then when a narrow beam is steered toward a long pulse extent, the beam shape (spatial filtering) may affect the signal (chirp) spectrum and introduce SNR losses. For the null-steering interference suppression, since normally deep nulls only correspond to spatial "points" in spatial filtering rather than "extents", it becomes evident that the resulting RASR loss may be more obvious. By assuming for the transmit signal a chirp with linear frequency modulation, frequency-dispersive beamforming can mitigate the effect of the pulse extension[20,22]. Under a linear approximation on steering angle vs. target delay, the ANS-beamformer implements a frequency-dependent beam steering using an embedded real-time FIR filter[7]. A constant time delay can be implemented using the embedded FIR filter without much resource occupation[7,24]. Rather than the normal purpose of removing frequency dispersion in a broadband beamforming[20], here the introduced time delay is to "make" the desired frequency dispersion to mitigate the PEL effect. However, since some essential approximations are involved, again, for null-steering interference suppression, the above PEL compensation may not be accurate enough to precisely disperse a null "point" to the whole pulse "extent" and make a perfect suppression[5,20].

An alternative separation approach employs a posteriori DBF in elevation on the ground, range-bin by range-bin after range compression[4,8,18]. By this way, no extra onboard computation is essential, and useful information about the spatial structure and enough DOFs will be preserved, enabling flexible and adaptive beamforming on the ground. It can avoid problems like topographic height variation. The performance improvements with adaptive DBF in presence of topographic height variations were verified in Ref. [8] and Ref. [23] for MWE-SAR and DBF-SAR case, respectively. Since there is no real-time beam scanning onboard the satellite, after range compres-

sion on the ground, the pulse extent is compressed to only one range bin, so that the PEL problem is also solved easily on the ground. The only critical issue is the choice on the number of receive elevation subapertures/channels under a given properly designed antenna height[8]. Using a large number of receive channels means a small subaperture size and a broad subaperture-level beam, and will preserve enough DOFs and achieve optimum performance, but it also bring on severe increase in the downloaded data volume. It is shown in Ref. [8] that the choice of receive subaperture number is restricted by multiple inherent constraints and trade-off has to be made between performance degradation and data volume increase. It is concluded that considering the performance preserving requirement as well as survey efficiency, a channel number of more than twice the transmit waveform number is required[8], which means a more than double data downlink rate requirement compared with the onboard ANS-DBF approach in Refs. [6,7]. If the receive subaperture number is equal to or just slightly larger than the transmit waveform number, severe performance degradations, especially the SNR and RASR loss at swath borders, will be unavoidable and unacceptable[8].

In this paper, the performance of a separation approach employing hybrid DBF in elevation[4,8,9] by combining the onboard real-time beamsteering and a posteriori DBF on the ground is elaborately investigated. The approach was originally suggested in Ref. [4] and its feasibility was briefly discussed in Ref. [8] and Ref. [9]. As a cascaded structure that comprises two subsequent DBF networks, the onboard real-time part effectuates the steering of the mainlobes for multiple partitioned groups of antenna elements in elevation to ensure sufficient signal receive gain for the multiple transmit waveforms over the whole range of the swath, but do nothing with the echo separation. In the meantime, essential DOFs and spatial structure information are preserved in the data of the output channels with a significantly reduced channel number. Since a much wider subaperture beam (compared to the full-aperture sharp beam in ANS-DBF) is employed with no need to place scanning nulls in real time, the topography and PEL problem can be self-relieved. The a posteriori adaptive DBF network (the ground part), after range compression, mainly performs the task of placing nulls bin-by-bin along range to cancel the range interference from other transmit waveforms, which enables flexible and adaptive beamforming to avoid the topographic height variation problem. The system performance on SNR and range ASR are theoretically analyzed and simulated in this paper. It is shown that the hybrid DBF approach in elevation can integrate the both advantages of the onboard ANS-beamforming and the a posteriori ground DBF.

2 System Concept Review

The basic idea of MWE-SAR is reviewed briefly in this section, which is originally proposed in Ref. [4] and later explained in more detail in Refs. [5–11]. The waveform schemes used by MWE SAR sensing are also introduced and discussed briefly.

2.1 Operation modes for azimuth MWE SAR

A variety of promising implementations of the MWE concept were suggested to achieve different goals, among which the Azimuth MWE (AMWE) is prominent to achieve high-resolution wide-swath imaging[4,6–8]. The AMWE modes are the focus of this paper, and other interesting modes like Elevation MWE (EMWE)[5] are not included.

In detail, there are two suggested modes during transmission, which are illustrated in Fig. 1. For the multi-beam mode shown in Fig. 1(a), multiple transmit subbeams in azimuth are formed with the full antenna azimuth aperture, each subbeam covers a portion of the full illuminated footprint and has its own transmit waveform, thereby the Doppler bandwidth within each subbeam is reduced. For the multi-phase-center mode shown in Fig. 1(b), the full antenna azimuth aperture is split into multiple subapertures and radiating multiple waveforms with the common scene illumination. In this way the spatial di-

versity from the multiple transmit phase centers along azimuth is achieved. Note that in both modes, on the slow-time scale, the transmit waveforms from different subapertures/subbeams are transmitted in parallel and lead to a simultaneous scene illumination. On the fast-time scale, however, either the simultaneous[10,11,14,15] or the sequential transmission[4,6–8] is possible, which will be discussed briefly in the following subsection.

In whatever cases above, echoes arising from the simultaneous scene illumination by these transmit waveforms are received by multiple receive antenna elements along both azimuth (see Fig. 2(a)) and elevation direction (see Fig. 2(b)), the whole receive antenna is a sufficiently extended 2-D array. The additional information from the multiple elevation receivers are employed to separate echoes from different transmit waveforms using DBF on receive in elevation[6–8], which equivalently provides the waveform orthogonality in azimuth dimension.

2.2 Transmit waveform scheme

The waveform design for multiple transmitters is an important issue in realizing the above AMWE-SAR system, which should ensure a reliable separation of the echoes that arise from the multiple transmit waveforms by combining DBF on receive in elevation.

The early proposed waveform scheme of MWE SAR is transmitting a set of mutually time shifted chirped subpulses Refs. [4,6–8]. A basic chirped pulse with duration T_{p} and FM rate K_{r} is

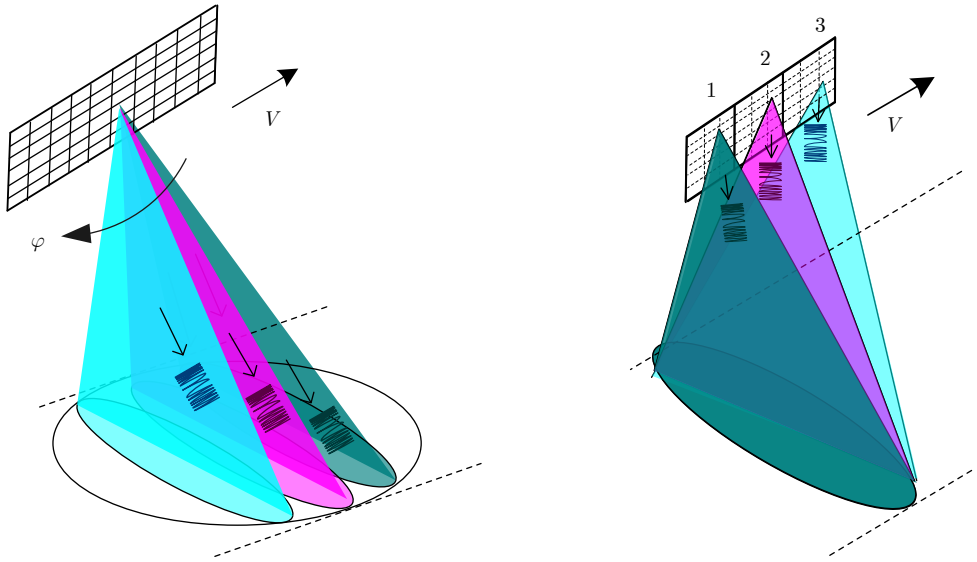

(a) Multi-beam mode (b) Multi-phase-center mode

Fig. 1 Azimuth MWE on transmit

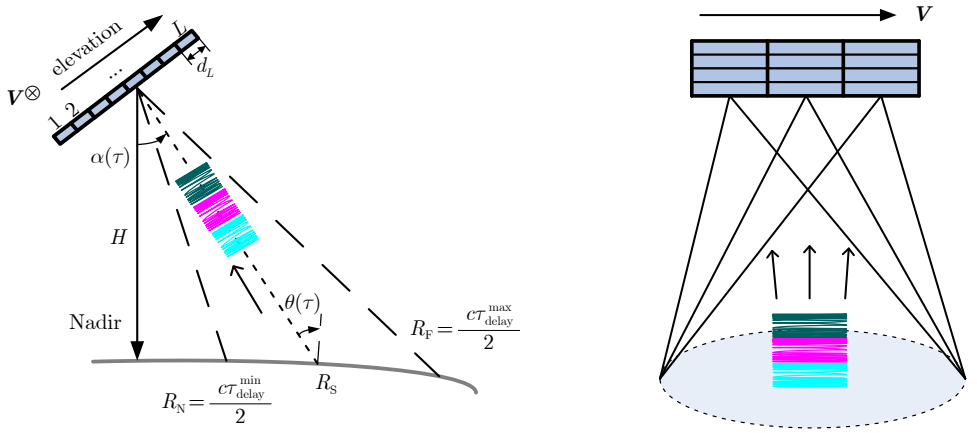

(a) Multi-channel receiving in elevation (b) Multi-channel receiving in azimuth

Fig. 2 Azimuth MWE on receive

$$p_0(t)=\mathrm{rect}\left(\frac{t}{T_\mathrm{p}}\right)\exp\left(\mathrm{j}\pi K_\mathrm{r}t^2\right) \tag{1a}$$

and the series of mutually time shifted waveforms are represented by

$$\begin{aligned}p_m(t)=&p_0(t-mT)=\mathrm{rect}\left(\frac{t-mT}{T_\mathrm{p}}\right)\\&\cdot\exp\left[\mathrm{j}\pi K_\mathrm{r}(t-mT)^2\right],\\&m=-\frac{M-1}{2},-\frac{M-1}{2}+1,\cdots,\ \frac{M-1}{2}\end{aligned} \tag{1b}$$

where T is the unit linearly shifted time and $T\geq T_\mathrm{p}$, which provides a sufficient mutual range delay that can be separated by DBF on receive in elevation. Note that here in order to give a unified form for both cases when M is odd or even, here the subscript value m, denoting the subpulse number, does not have to be an integer itself (m is increased by integers).

By merely switching between different antenna beams or subaperture elements during each transmitted subpulse, the generation of the time-shifted chirped subpulses is quite simple. As an alternative, the Short-Term Shift-Orthogonal (STSO) waveforms was proposed[11]. The linear time shift in Eq. (1b) is replaced by cyclical time shift to ensure the simultaneous transmission via multiple orthogonal transmit channels. Owing to the cyclical time shift, the transmitted signals from any two different channels will fulfill the following short-term shift orthogonality[11]

$$\int h(t,\tau)p_i^*(t)\cdot p_j(t+\tau)\mathrm{d}t=0\ \forall\ \tau\in\left[-\frac{\tilde{T}}{2},\frac{\tilde{T}}{2}\right],\ \ i\neq j \tag{2}$$

where $\tilde{T}$ is the basic cyclically shifted time, $h(t,\tau)$ represents a weighting function[11]. If $T=\tilde{T}$, it is obvious that the linear time-shifted subpulses also fulfill the requirement of Eq. (2), therefore Eq. (1) can be regarded as a specific kind of STSO waveforms.

2.3 Default assumption in this paper

For conciseness, in this paper, the analytical derivation and simulation are dedicated to the AMWE SAR mode with multiple azimuth subbeams on transmit. Owing to the similar transmit/receive antenna architecture in elevation dimension, the multi-waveforms separation manner here is also feasible for the multi-phase-center mode[4] if the same time-shifted chirped waveforms given in Eq. (1) is also used. If STSO waveform encoding scheme is used, due to the similar chirped-pulse-based signal structure, the method presented in this paper will also be feasible after some necessary modifications.

For an AMWE SAR system with M azimuth subbeams on transmit as shown in Fig. 1, M transmit waveforms are transmitted in every pulse repetition interval (PRI, denoted as T_r), each corresponding to a subbeam. The complex form of the overall transmit signal is represented by

$$\begin{aligned}s(t)=&\left[\left(\sum_{m=-\frac{M-1}{2}}^{\frac{M-1}{2}}p_m(t)\right)\otimes\left(\sum_{k=-\infty}^{\infty}\delta(t-kT_\mathrm{r})\right)\right]\\&\times\exp\left(\mathrm{j}2\pi f_\mathrm{c}t\right)\end{aligned} \tag{3a}$$

where f_c is the carrier frequency, k is the PRI number, $\delta(t)$ represents Dirac function, and $\otimes$ denotes time domain convolution. When a set of mutually time-shifted chirped subpulses described by Eq. (1) are used, $s(t)$ can be further represented by

$$\begin{aligned}s(t)=&\left[p_0(t)\otimes\left(\sum_{m=-\frac{M-1}{2}}^{\frac{M-1}{2}}\delta\left(t-mT\right)\right)\right.\\&\left.\otimes\left(\sum_{k=-\infty}^{\infty}\delta(t-kT_\mathrm{r})\right)\right]\times\exp\left(\mathrm{j}2\pi f_\mathrm{c}t\right)\end{aligned} \tag{3b}$$

As for the imaged scene in presence of topographic height variations, like the assumption used in Ref. [8], we consider an instantaneously illuminated swath characterized, along the iso-range lines, by a homogeneous backscattering surface and constant topographic height. This means that in elevation the layover effect does not occur, and in azimuth, a mean height of all contributing backscattering within the illuminated azimuth extend is sufficiently representative. Though simple, this reference surface allows for a first stage comparison for achievable performance in the simulation of this paper.

3 Cascaded Digital Beamforming Networks in Elevation

3.1 Structure and signal model of cascaded DBF networks

The structure of cascaded DBF networks in elevation investigated in this paper is given by Fig. 3. The total receive aperture in elevation is split into L_0 subapertures. The size of each subaperture is d_0. In the following of this paper, each subaperture with size d_0 is called an "antenna element". Due to the relatively small scan angle needed for the onboard beamforming, the element spacing d_0 is not restricted by half wavelength[7]. With a properly designed antenna height[4,8], a larger d_0 can reduce the element number L_0, which is pre-requisite considering the downloaded data volume for a system employing a posteriori DBF only on the ground[8]; However, this will also narrow the beam of each antenna element. In this paper, since an onboard DBF network is used and the downloaded data volume is no longer dependent on L_0, d_0 should be small enough so that a near constant element-level gain within the swath can be held.

For each antenna element, the signal is received, demodulated and digitized separately. As shows in Fig. 2 and Fig. 3, suppose that the first element is selected as the reference channel in elevation, according to Eq. (3), the baseband echo of the mth subpulse $p_m(t)$ in the kth PRI received by the reference elevation channel after coherent demodulation is given by

$$\begin{aligned} s_m^{(k)}(t) &= \int_{-\infty}^{\infty} g_m^{(k)}(\tau) p_m\left(t-\tau-kT_{\mathrm{r}}\right) \mathrm{d}\tau \\ &= \int_{-\frac{T_{\mathrm{p}}}{2}}^{\frac{T_{\mathrm{p}}}{2}} g_m^{(k)}(t-\xi-mT-kT_{\mathrm{r}}) p_0(\xi)\, \mathrm{d}\xi \end{aligned} \quad (4)$$

where $g_m^{(k)}(\tau)$ is the extended ground reflectivity within the illuminated patch[8] of the mth subpulse in the kth PRI, $\tau \in \left[\tau_{\mathrm{delay}}^{\min}, \tau_{\mathrm{delay}}^{\max}\right]$ is the round-trip delay from ground scatterer to the reference channel, with its delay center value $\tau_{\mathrm{c}} = \left(\tau_{\mathrm{delay}}^{\max} + \tau_{\mathrm{delay}}^{\min}\right)/2$ (cf., Fig. 2); $\xi \in [-T_{\mathrm{p}}/2,\ T_{\mathrm{p}}/2]$ represents the relative in-pulse time.

Note that here τ also represents the slant-range position on the ground, so that the off-nadir angle α and incidence θ in Fig. 2 can be represented as single-valued functions of delay if ignoring

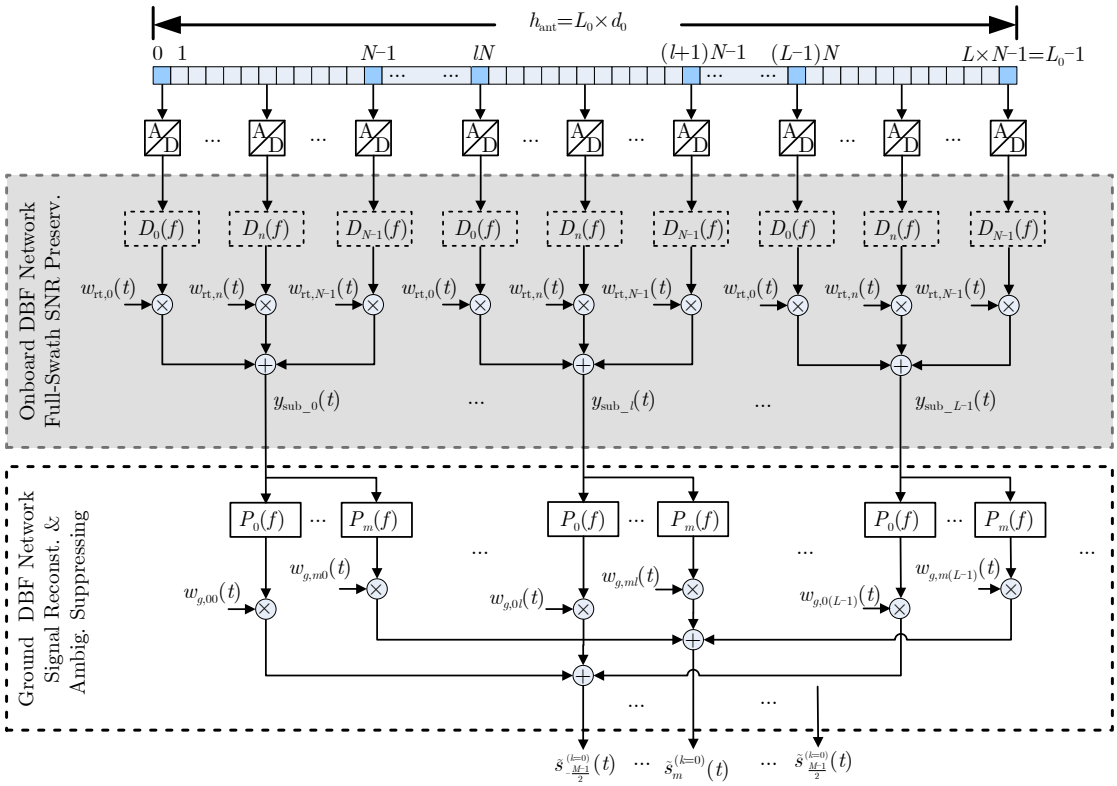

Fig. 3 Cascaded DBF networks in elevation performing the SNR-preserving and interferences-free signal separation

layover effect, according to the basic assumption given in Section 2.3. To a first approximation, these functions can be determined from the orbit and the given Earth model[6], however, their true values cannot be simply modeled. Also note that in order to give a concise form, the transmit antenna pattern and the receive element-level pattern are included in $g_m^{(k)}(\tau)$. A detailed description for $g_m^{(k)}(\tau)$ under the homogeneous white reflectivity assumption can be found in Ref. [8]. For the l_0th antenna element, the demodulated echo of the same subpulse can be expressed in a similar integral form as

$$s_{m,l_0}^{(k)}\left(t'=t+\Delta\tau_{l_0}\right)=\int_{-\frac{T_\mathrm{p}}{2}}^{\frac{T_\mathrm{p}}{2}} g_m^{(k)}\left(t'-\xi-mT-kT_\mathrm{r}\right)\cdot\exp\left[\mathrm{j}2\pi f_\mathrm{c} l_0\Delta\tau_m^{(k)}(t'-\xi)\right]p_0(\xi)\,\mathrm{d}\xi \tag{5}$$

In comparison with Eq. (4), there is an extra demodulated phase term introduced by the additional trip delay $l_0\cdot\Delta\tau_m^{(k)}$, which is given by

$$\Delta\tau_m^{(k)}(\zeta)=\frac{d_0\sin\left[\alpha\left(\tau=\zeta-mT-kT_\mathrm{r}\right)-\alpha_0\right]}{\mathrm{c}}\triangleq\frac{d_0\sin\left[\beta\left(\tau=\zeta-mT-kT_\mathrm{r}\right)\right]}{\mathrm{c}} \tag{6}$$

where α_0 is the off-nadir angle of the antenna normal boresight, β is the off-normal direction angle, c is the speed of light. Besides the above phase shift, there still exists a small envelope delay $\Delta\tau_{l_0}\approx l_0\Delta\tau_m^{(k)}(\tau_\mathrm{c})$ for the receive time. The envelope shift $\Delta\tau_{l_0}$ can be ignored[6–8] if the signal bandwidth is not wider than the array bandwidth[20], which is the usual case for most current spaceborne SAR using phased array method. In this paper, this conventional phase-shift DBF case with narrowband signal is assumed, therefore, in the following expressions $t'=t$ is adopted. In a very high-resolution case, however, such an approximation may cause frequency dispersion phenomenon in beamforming if the signal bandwidth is much wider than the array bandwidth[20]. Then a time-varying time-delay network implemented by FIR filtering, or specially designed subband-based scalloped beamforming is essential to fulfill broadband DBF compensation. One can find a detailed description for this issue in Ref. [20].

As shown in Fig. 3, the L_0 antenna elements are then partitioned into L groups, each group has N elements and forms a larger subaperture with the size $N\times d_0$. In the following, a subaperture refers in particular to such a group of antenna elements. In general the overlapping of subapertures is permissible, but it is not considered here for simplification. Let $s_{m,ln}^{(k)}(t)$ denote the echo from the mth transmit subpulse in the kth PRI received by the nth element (n=0, 1, ⋯, $N-1$) within the lth subaperture (l=0, 1, ⋯, $L-1$), according to Eq. (5), $s_{m,ln}^{(k)}(t)$ can be further expressed as

$$\begin{aligned}s_{m,ln}^{(k)}(t)=&\exp\left[\mathrm{j}2(lN+n)\pi f_\mathrm{c}\Delta\tau_m^{(k)}(t)\right]\\&\cdot\int_{-\frac{T_\mathrm{p}}{2}}^{\frac{T_\mathrm{p}}{2}} g_m^{(k)}(t-\xi-mT-kT_\mathrm{r})\\&\cdot\exp\left[\mathrm{j}2(lN+n)\pi f_\mathrm{c}\cdot\delta_{\Delta\tau_m^{(k)}}(\xi;t)\right]p_0(\xi)\,\mathrm{d}\xi\end{aligned} \tag{7}$$

where

$$\delta_{\Delta\tau_m^{(k)}}(\xi;t)=\Delta\tau_m^{(k)}(t-\xi)-\Delta\tau_m^{(k)}(t) \tag{8}$$

The time-variant exponential terms outside the integral in Eq. (7) for each receive elements are always connected to the center look angle of the given subpulse at a given time, which constitute the time-variant steering vector associated with that subpulse and further determine the time-variant weighting vector of the scanning beam in Refs. [6,7]. However, the exponential term containing $\delta_{\Delta\tau_m^{(k)}}(\xi;t)$ inside the integral is dependent on the intra-pulse time variable ξ, which will make an unwanted intra-pulse element-dependent phase weighting in the pulse extend $-T_\mathrm{p}/2\le\xi<T_\mathrm{p}/2$ and cause PEL at $\xi\neq0$. This problem can be easily solved in the a posteriori DBF approach by range compression. In Appendix A, a summary derivation of the post-range-compression approach is reviewed as in Ref. [8], wherea full form of the received signal vector $\boldsymbol{X}_{\mathrm{comp,sub\_}l}(t)$ can be written in matrix form as[8]

$$\boldsymbol{X}_{\mathrm{comp,sub\_}l}(t)=\sum_{k=-\infty}^{\infty}\boldsymbol{A}^{(k)}(t)\boldsymbol{s}_{\mathrm{comp,sub\_}l}^{(k)}(t) \tag{9}$$

The above compact linear signal model is used to develop DBF methods in Ref. [8] for re-

constructing the unambiguous signal $\boldsymbol{s}^{(0)}_{\mathrm{comp,sub\_}l}(t)$ from $\boldsymbol{X}_{\mathrm{comp,sub\_}l}(t)$. However, for the non-range-compressed raw data in Eq. (7) onboard the satellite, if the phase value $\delta_{\Delta\tau_m^{(k)}}(\xi)$ is also directly omitted within the uncompressed pulse duration, the influence of PEL may deteriorate the system performance. Therefore, here the lth-subaperture input signal (including the additive noise) of the first-stage beamformer will firstly be written in its initial form given by the following Eq. (10), later we will re-derive a similar model like Eq. (9) for the range-uncompressed signal in Section 3.2.3.

$$\boldsymbol{x}_{\mathrm{sub\_}l}=\sum_{k=-\infty}^{\infty}\sum_{m=-\frac{M-1}{2}}^{\frac{M-1}{2}}\boldsymbol{s}^{(k)}_{m,\mathrm{sub\_}l}(t)+\boldsymbol{\eta}_{\mathrm{sub\_}l}(t) \tag{10a}$$

$$\left.\begin{aligned}\boldsymbol{x}_{\mathrm{sub\_}l}(t)&=\left[x_{l0}(t),x_{l1}(t),\cdots,x_{ln}(t),\cdots,x_{l(N-1)}(t)\right]^{\mathrm{T}}\\ \boldsymbol{s}^{(k)}_{m,\mathrm{sub\_}l}(t)&=\left[s^{(k)}_{m,l0}(t),s^{(k)}_{m,l1}(t),\cdots,s^{(k)}_{m,ln}(t),\right.\\ &\qquad\left.\cdots,s^{(k)}_{m,l(N-1)}(t)\right]^{\mathrm{T}}\\ \boldsymbol{\eta}_{\mathrm{sub\_}l}(t)&=\left[\eta_{l0}(t),\eta_{l1}(t),\cdots,\eta_{ln}(t),\cdots,\eta_{l(N-1)}(t)\right]\end{aligned}\right\} \tag{10b}$$

In Eq. (10) $\eta_{ln}(t)$ is the additive noise of the nth element in the lth subaperture. The main purpose of the first-stage onboard DBF within each subaperture is to optimize signal power of the multiple transmit waveforms/subpulses for improved SNR performance over the whole swath. At the same time, the output data volume can be N-times reduced onboard the satellite.

By combining the N elements of the vector $\boldsymbol{x}_{\mathrm{sub\_}l}$ within each subaperture, the output of each subaperture is a scalar signal denoted as $y_{\mathrm{sub\_}l}(t)$. The output signals $y_{\mathrm{sub\_}l}(t)$ (l=0, 1, $\cdots$,$L-1$) from different subapertures constitute the input vector of the second stage cascaded DBF network

$$\boldsymbol{Y}_{\mathrm{sub}}(t)=\left[y_{\mathrm{sub\_}0}(t),\cdots,y_{\mathrm{sub\_}l}(t),\cdots,y_{\mathrm{sub\_}L-1}(t)\right]^{\mathrm{T}} \tag{11}$$

In this stage null-steering DBF is performed on the ground to realize the reliable extraction of echoes from M transmit subpulses, *i.e.* $s^{(0)}_{-\frac{M-1}{2}}(t)$ to $s^{(0)}_{\frac{M-1}{2}}(t)$, free of mutual interferences, by flexibly and adaptively placing nulls of the array pattern.

Both the onboard realtime ANS beamformer in Ref. [7] and the ground a posteriori DBF in Ref. [8] can be viewed as special cases of the hybrid cascaded DBF networks in Fig. 3. For the onboard ANS DBF network[7], the second-stage DBF in Fig. 3 is omitted; in the onboard part, now the number of the onboard beamformers is L=M, and the number of the elements within each beamformer is $N=L_0$. It means that each "subaperture" here is extended to the full aperture and mutually overlaps completely. For the ground a posteriori DBF network[8], it can be considered that there are $L=L_0$ subapertures in the onboard DBF network, and each subaperture beamformer only has one antenna element and acts as a direct through connection filter.

3.2 Onboard SNR-Preserving DBF

In order to optimize the overall signal power and minimize signal distortion over the whole swath in each subaperture onboard the satellite, a properly designed digital subaperture beam, which is much wider than the full-aperture sharp beam in ANS-DBF[7], should be formed and follow the multiple radar subpulses as a whole when they travel on the ground, keeping enough high receive gain within the entire instantaneous scattering field at any instance of time. For onboard DBF, the off-normal direction angle $\beta(\tau)$ has to be predetermined by a assumed model. Fortunately, here the formed subaperture beam is much wider and no deep null is needed, the accuracy demand for $\beta(\tau)$ is not high.

Given a pulse duration T, the ground range pulse extent $\chi_{rg}(T,\beta)$ and corresponding angular pulse extent $\chi_{\beta}(T,\beta)$ can be calculated and their expressions have been given in Ref. [21]. For a MWE SAR system, since the whole transmit duration is $M\times T$, the instantaneous angular pulse extent covering the entire instantaneous scattering field becomes $\chi_{\beta}(M\cdot T,\beta(\tau))$. In Ref. [8] it has been analyzed that if the subaperture number $L>M$, it will not be difficult for a system designer to have a nominal 3 dB-beamwidth of each subaperture larger than $\chi_{\beta}(M\cdot T,\beta(\tau))$, so that the PEL influence is comparatively limited.

3.2.1 Beamformer design for instantaneous scattering field

This subsection aims at optimizing the DBF weighting $\bar{\boldsymbol{w}}_{\mathrm{RT}}$ for the instantaneous scattering field at the center of the swath, *i.e.* $t=\tau_{\mathrm{c}}$. Let $\beta_0=\chi_\beta\left[M\cdot T,\beta_{\mathrm{c}}=\beta(\tau_{\mathrm{c}})\right]/2$, representing the half angular pulse extent at τ_{c}. With a given weighting vector $\bar{\boldsymbol{w}}_{\mathrm{RT}}^{\mathrm{H}}$, the array pattern function of an antenna subaperture can be written as

$$\left.\begin{aligned} &B(\psi)=\bar{\boldsymbol{w}}_{\mathrm{RT}}^{\mathrm{H}}\boldsymbol{I}_{\mathrm{s}}(\psi_{\mathrm{c}})\boldsymbol{v}_\psi(\psi-\psi_{\mathrm{c}})\triangleq\bar{\boldsymbol{w}}_{\mathrm{RT},\psi_{\mathrm{c}}}^{\mathrm{H}}\\ &\boldsymbol{v}_\psi(\psi'=\psi-\psi_{\mathrm{c}})\end{aligned}\right\} \tag{12}$$

$$\boldsymbol{v}_\psi(\psi)=\left[\begin{array}{cccc}1 & \mathrm{e}^{\mathrm{j}\psi} & \cdots & \mathrm{e}^{\mathrm{j}(N-1)\psi}\end{array}\right]^{\mathrm{T}} \tag{13}$$

where $\psi=2\pi\dfrac{d_0\sin\beta}{\lambda}$ and $\psi_{\mathrm{c}}=2\pi\dfrac{d_0\sin\beta_{\mathrm{c}}}{\lambda}$, $\boldsymbol{I}_{\mathrm{s}}(\psi_{\mathrm{c}})=\mathrm{diag}\left[\boldsymbol{v}_\psi(\psi_{\mathrm{c}})\right]$ is the $N\times N$ steering diagonal matrix for the direction ψ_{c}. The angular region $[-\beta_0,\beta_0]$ covering the angular pulse extent $\chi_\beta\left[M\cdot T,\beta_{\mathrm{c}}=\beta(\tau_{\mathrm{c}})\right]$ will correspond to a ψ-domain region $\psi'\in[-\psi_0,\psi_0]$, where $\psi_0=2\pi\dfrac{d_0\sin\beta_0}{\lambda}$. Assuming that an "ideal" antenna pattern $B_{\mathrm{d}}(\psi')$ is given, which has the optimum response in the angular region $[-\psi_0,\psi_0]$, *e.g.*, fulfilling

$$B_{\mathrm{d}}(\psi')=1,\quad -\psi_0\le\psi'\le\psi_0 \tag{14}$$

It is evident that if Eq. (14) is satisfied, the spatial filtering within the instantaneous pulse extent is fixed-gain and no amplitude modulation and relevant losses will be introduced on each subpulse. In other words, it is an intra- and inter-subpulse distortionless "optimum" spatial filter. The following square error is defined by

$$e=\int_{-\psi_0}^{\psi_0}\left|B_{\mathrm{d}}(\psi')-\bar{\boldsymbol{w}}_{\mathrm{RT},\psi_{\mathrm{c}}}^{\mathrm{H}}\boldsymbol{v}_\psi(\psi')\right|^2\mathrm{d}\psi' \tag{15}$$

Based on the "zero gradient" method the following constraint equation is derived:

$$\boldsymbol{Q}_{\psi_0}\bar{\boldsymbol{w}}_{\mathrm{RT},\psi_{\mathrm{c}}}=\boldsymbol{b} \tag{16}$$

where

$$\boldsymbol{Q}_{\psi_0}=\int_{-\psi_0}^{\psi_0}\boldsymbol{v}_\psi(\psi')\boldsymbol{v}_\psi^{\mathrm{H}}(\psi')\mathrm{d}\psi' \tag{17}$$

$$\boldsymbol{b}=\int_{-\psi_0}^{\psi_0}\boldsymbol{v}_\psi(\psi')B_{\mathrm{d}}^*(\psi')\mathrm{d}\psi' \tag{18}$$

It is easy to derive that $\boldsymbol{Q}_\pi=2\pi\boldsymbol{I}_N$, $\boldsymbol{I}_N$ is a N-dimensional identity matrix. It implies that if the subaperture pattern control is performed on the whole unambiguous region $[-\pi,\pi]$, then $\boldsymbol{Q}_{\psi_0}$ is a full rank matrix, no remaining DOFs are available to further optimize the signal-to-noise level. Fortunately, Here the constraint is given in a small angular region $[-\psi_0,\psi_0]$, eigenvalues of $\boldsymbol{Q}_{\psi_0}$ will drop down quickly. If only the principal components in eigen-space of $\boldsymbol{Q}_{\psi_0}$ are used to the form the constraint Eq. (16), then more DOFs are available for subaperture-level SNR optimization. The principal-component version of $\boldsymbol{Q}_{\psi_0}$ can be written as

$$\widehat{\boldsymbol{Q}}_{\psi_0}=\sum_{l=0}^{N_{\mathrm{p}}-1}\lambda_l\boldsymbol{\phi}_l\boldsymbol{\phi}_l^{\mathrm{H}}=\boldsymbol{U}_{\boldsymbol{Q}_{\mathrm{s}}}\Sigma_{\boldsymbol{Q}_{\mathrm{s}}}\boldsymbol{U}_{\boldsymbol{Q}_{\mathrm{s}}}^{\mathrm{H}} \tag{19}$$

where $\Sigma_{\boldsymbol{Q}_{\mathrm{s}}}$ is the diagonal matrix comprising N_{p} principal eigenvalues of $\boldsymbol{Q}_{\psi_0}$, *i.e.* λ_0 to $\lambda_{N_{\mathrm{p}}-1}$, $\boldsymbol{U}_{\boldsymbol{Q}_{\mathrm{s}}}$ is the signal-subspace matrix comprising N_{p} principal eigenvectors correspondingly. N_{p} is selected by a trade-off between minimizing square error e and the available DOFs for performance further SNR optimization, it is determined in this paper as

$$N_{\mathrm{p}}=2\times\mathrm{round}\left[\frac{\psi_0}{2\pi}N+k_{\mathrm{p}}\right] \tag{20}$$

where k_{p} is a turning parameter and its value is set as 1 here. By using the principal component method, the constraint Eq. (16) can be rank-reduced and converted to

$$\boldsymbol{U}_{\boldsymbol{Q}_{\mathrm{s}}}^{\mathrm{H}}\bar{\boldsymbol{w}}_{\mathrm{RT},\psi_{\mathrm{c}}}=\Sigma_{\boldsymbol{Q}_{\mathrm{s}}}^{-1}\boldsymbol{U}_{\boldsymbol{Q}_{\mathrm{s}}}^{\mathrm{H}}\boldsymbol{b}\triangleq\boldsymbol{g}_{\mathrm{ESLC}} \tag{21}$$

Under the above Eigen-Space Linear Constraint (ESLC) set, by exploiting the rest subaperture DOFs to keep minimum output noise power, one can derive the following weight vector as

$$\bar{\boldsymbol{w}}_{\mathrm{RT}}^{\mathrm{H}}=\bar{\boldsymbol{w}}_{\mathrm{ESLC}}^{\mathrm{H}}=\boldsymbol{g}_{\mathrm{ESLC}}^{\mathrm{H}}\left(\boldsymbol{U}_{\boldsymbol{Q}_{\mathrm{s}}}^{\mathrm{H}}\boldsymbol{U}_{\boldsymbol{Q}_{\mathrm{s}}}\right)^{-1}\boldsymbol{U}_{\boldsymbol{Q}_{\mathrm{s}}}^{\mathrm{H}}\boldsymbol{I}_{\mathrm{s}}(-\psi_{\mathrm{c}}) \tag{22}$$

It is evident that $\bar{\boldsymbol{w}}_{\mathrm{ESLC}}^{\mathrm{H}}$ is a distortionless-response preferred beamformer that N_{p} subaperture-level DOFs are spent to keep distortionless response. The cost may be a degree of signal power gain loss. In practice, however, the distortionless response constraint is not a mandatory one. For a SAR system, some degree of mild signal distortion is normally allowable and can be compensated in the a posteriori data processing, however, SNR loss is irretrievable. Considering above factors, in some appropriate sense, our new objective is to maximize the signal response while simultaneously minimizing the response due to

noise and interferences. In Appendix B, an applicable way is derived and a new weight vector $\bar{\boldsymbol{w}}_{\mathrm{RT}}=\bar{\boldsymbol{w}}_{\mathrm{DPSS}}$ is given to minimize the SNR loss.

It is clear that the above weight vectors are designed only exploring information of the total instantaneous pulse extent, other prior information about the signal time-frequency relation is not considered. This type is called as Type-A beamforming in this paper. In the following subsection 3.2.3, another Type-B beamforming will be introduced.

3.2.2 Beam scanning and subaperture-level output

In theory, it is possible to optimize the real-time weighting vector $\boldsymbol{w}_{\mathrm{RT}}^{\mathrm{H}}(t)$ at any instance of time t. Due to the normally small scan angle needed for the onboard beamforming, $\chi_{\beta}\left[M\cdot T,\beta(t)\right]$ only changes slightly with t. By utilizing the relationship expressed in Eq. (A-5) for the pulse-centred steering vectors, the real-time scanning subaperture-level beam can be practically designed with two steps: first, a "static" beamformer (corresponding to $\bar{\boldsymbol{w}}_{\mathrm{RT}}$ in the previous subsection) is optimized aimed at the instantaneous scattering field $[-\beta_0,\beta_0]$ (may leaving some margin for β_0) at the swath center, then a real-time scanning is added to chase the whole pulses. Accordingly, the time-variant weighting vector, after the real-time scanning is added, can be represented by

$$\boldsymbol{w}_{\mathrm{RT}}^{\mathrm{H}}(t)=\bar{\boldsymbol{w}}_{\mathrm{RT}}^{\mathrm{H}}\boldsymbol{\Lambda}^{\mathrm{H}}(t) \tag{23}$$

where the $N\times N$ dynamic steering diagonal matrix $\boldsymbol{\Lambda}^{\mathrm{H}}(t)$ is defined by Eq. (A-6).

According to the input signal model given by Eq. (10), the output signal of the lth subaperture is then given by

$$\begin{aligned} y_{\mathrm{sub}\_l}(t) &= \boldsymbol{w}_{\mathrm{RT}}^{\mathrm{H}}(t)\boldsymbol{x}_{\mathrm{sub}\_l}(t) \\ &= \sum_{k=-\infty}^{\infty}\sum_{m=-\frac{M-1}{2}}^{\frac{M-1}{2}} s_{m,\mathrm{sub}\_l}^{(k),\,\mathrm{out}}(t)+\eta_{\mathrm{sub}\_l}^{\mathrm{out}}(t) \end{aligned} \tag{24a}$$

$$\left.\begin{aligned} s_{m,\mathrm{sub}\_l}^{(k),\,\mathrm{out}}(t) &= \boldsymbol{w}_{\mathrm{RT}}^{\mathrm{H}}(t)\boldsymbol{s}_{m,\mathrm{sub}\_l}^{(k)}(t) \\ \boldsymbol{\eta}_{\mathrm{sub}\_l}^{\mathrm{out}}(t) &= \boldsymbol{w}_{\mathrm{RT}}^{\mathrm{H}}(t)\boldsymbol{\eta}_{\mathrm{sub}\_l}(t) \end{aligned}\right\} \tag{24b}$$

According to the expression of $\boldsymbol{w}_{\mathrm{RT}}^{\mathrm{H}}(t)$ and $\boldsymbol{s}_{m,\mathrm{sub}\_l}^{(k)}(t)$, $s_{m,\mathrm{sub}\_l}^{(k),\,\mathrm{out}}(t)$ can be further written as

$$\begin{aligned} s_{m,\mathrm{sub}\_l}^{(k),\,\mathrm{out}}(t) &= \sum_{n=0}^{N-1} s_{m,ln}^{(k)}(t)\cdot\left[\boldsymbol{w}_{\mathrm{RT}}^{\mathrm{H}}(t)\right]_n \\ &= \left\{g_m^{(k)}(t-mT-kT_{\mathrm{r}})\right. \\ &\quad \left.\cdot\exp\left[\mathrm{j}2lN\pi f_{\mathrm{c}}\Delta\tau_m^{(k)}(t)\right]\right\}\otimes\widehat{p}_{0,m}^{(k)}(t) \end{aligned} \tag{25}$$

where

$$\begin{aligned} \widehat{p}_{0,m}^{(k)}(t) &= p_0(t)\times\sum_{n=0}^{N-1}\left[\chi_{mn}^{(k)}\exp\left(-\mathrm{j}2n\pi f_{\mathrm{b}}t\right)\right] \\ &\triangleq p_0(t)\,\mu_m^{(k)}(t),\quad -\frac{T_{\mathrm{p}}}{2}\le t\le\frac{T_{\mathrm{p}}}{2} \end{aligned} \tag{26}$$

In Eq. (26) the serial $\chi_{mn}^{(k)}$ is

$$\chi_{mn}^{(k)}=\left[\bar{\boldsymbol{w}}_{\mathrm{RT}}\right]_n\cdot\exp\left[\mathrm{j}2n\pi f_{\mathrm{c}}\Delta\tau_m^{(k)}(\tau_{\mathrm{c}})\right] \tag{27}$$

and the function $\mu_m^{(k)}(t)$ can be calculated from the serial $\chi_{m,l}^{(k)}$ using the fast Chirp Z-transform[25]. It is clear from Eq. (27) that $\mu_m^{(k)}(t)$ is the weighting function caused by the time-variant subaperture gain over the extent of the mth transmit subpulse in the kth PRI, it also can be regarded as the intra-subpulse distortion. In Section 5, the plots of $\mu_m^{(k)}(t)$ for the distortionless-response-preferred weighting $\bar{\boldsymbol{w}}_{\mathrm{ESLC}}^{\mathrm{H}}$ and the SNR-preferred $\bar{\boldsymbol{w}}_{\mathrm{DPSS}}$ will be compared.

3.2.3 Alternative approach exploring subpulse structure information

If the prior information of the chirped subpulse time-frequency structure is utilized, the received echo $s_{m,ln}^{(k)}(t)$ given by Eq. (7) can be further rewritten as

$$\begin{aligned} s_{m,ln}^{(k)}(t) &= \exp\left[\mathrm{j}2(lN+n)\pi f_{\mathrm{c}}\Delta\tau_m^{(k)}(t)\right] \\ &\quad\cdot\int_{-\frac{T_{\mathrm{p}}}{2}}^{\frac{T_{\mathrm{p}}}{2}} g_m^{(k)}(t-\xi-mT-kT_{\mathrm{r}}) \\ &\quad\cdot\exp\left\{\mathrm{j}2(lN+n)\pi f_{\mathrm{c}}\delta_{\Delta\tau_m^{(k)}}(\xi;t)\right\} \\ &\quad\cdot\exp\left(\mathrm{j}\pi K_{\mathrm{r}}\xi^2\right)\mathrm{d}\xi \\ &\approx \exp\left[\mathrm{j}2(lN+n)\pi f_{\mathrm{c}}\Delta\tau_m^{(k)}(t)\right] \\ &\quad\cdot\int_{-\frac{T_{\mathrm{p}}}{2}}^{\frac{T_{\mathrm{p}}}{2}} g_m^{(k)}(t-\xi-mT-kT_{\mathrm{r}}) \\ &\quad\cdot\exp\left\{-\mathrm{j}2(lN+n)\pi f_{\mathrm{b}}\xi\right\}\exp\left(\mathrm{j}\pi K_{\mathrm{r}}\xi^2\right)\mathrm{d}\xi \end{aligned} \tag{28}$$

In Eq. (28) we use the linear relationship between the off-boresight angle and echo delay[6–8,22] implied in Eq. (A-7), so that $\delta_{\Delta\tau_m^{(k)}}(\xi;t)$ can be ap-

proximated as a linear phase term corresponding to a frequency shift $(lN+n)f_{\mathrm{b}}$. By exploiting the relationship of a LFM signal between time-domain and frequency-domain shift, within each subaperture, one can approximate the nth-element signal $s_{m,ln}^{(k)}(t)$ with the time-shift version of its subaperture-level reference signal $s_{m,l0}^{(k)}(t)$ as

$$\begin{aligned} s_{m,ln}^{(k)}(t) &= \exp\left(\mathrm{j}\pi\frac{n^2 f_{\mathrm{b}}^2}{K_{\mathrm{r}}}\right)\exp\left[\mathrm{j}2n\pi f_{\mathrm{c}}\Delta\tau_m^{(k)}(t-nT_{\mathrm{b}})\right] \\ &\quad\cdot s_{m,l0}^{(k)}(t-nT_{\mathrm{b}}) \\ &\approx \exp\left[\mathrm{j}2n\pi f_{\mathrm{c}}\Delta\tau_m^{(k)}(t-nT_{\mathrm{b}})\right]\times s_{m,l0}^{(k)}(t-nT_{\mathrm{b}}) \end{aligned} \tag{29}$$

where

$$T_{\mathrm{b}} = \frac{f_{\mathrm{b}}}{K_{\mathrm{r}}} \tag{30}$$

is the equivalent time shift coupled with the frequency shift f_{b}. For brevity, the phase term $\exp\left(\mathrm{j}\pi\frac{n^2 f_{\mathrm{b}}^2}{K_{\mathrm{r}}}\right)$ is neglected since it is small and can be easily compensated. From Eq. (29) it is found that owing to the same linear connection between time and frequency within each chirped subpulse, the additional intra-pulse phase shift $-2n\pi f_{\mathrm{b}}\xi$ (relative to the reference channel) varying linearly over the subpulse extent can be equivalent to a relative time delay nT_{b}. It should be noted that now the FIR interpolation filtering (see the optional filters $D_n(f)$ in Fig. 3) is essential, and the first step of the onboard network is to implement the following linear frequency-dependent phase shifts within each group of antenna elements

$$D_n(f) = 2n\pi f T_{\mathrm{b}},\quad n=0,1,2,\cdots,N-1 \tag{31}$$

which introduce different time delays in the signal paths of the individual antenna elements within each subaperture prior to the following beamforming, to make the beamforming frequency-dispersive and mitigate the effect of the pulse extension. After this step, the input signal vector $\boldsymbol{x}_{\mathrm{sub}\_l}$ in Eq. (10) now becomes

$$\begin{aligned} \boldsymbol{x}_{\mathrm{sub}\_l}^{\mathrm{shift}}(t) = [&x_{0l}(t), x_{l1}(t+T_{\mathrm{b}}),\cdots,x_{ln}(t+nT_{\mathrm{b}}), \\ &\cdots, x_{l(N-1)}(t+(N-1)T_{\mathrm{b}})]^{\mathrm{T}} \end{aligned} \tag{32}$$

and according to Eq. (30) can be further written in matrix form as

$$\boldsymbol{x}_{\mathrm{sub}\_n}^{\mathrm{shift}}(t) = \sum_{k=-\infty}^{\infty}\boldsymbol{A}^{(k)}(t)\boldsymbol{s}_{\mathrm{sub}\_l}^{(k)}(t) + \boldsymbol{\eta}_{\mathrm{sub}\_l}(t) \tag{33}$$

where $\boldsymbol{s}_{\mathrm{sub}\_l}^{(k)}(t) = \left[s_{-\frac{M-1}{2},l0}^{(k)},\cdots,s_{m,l0}^{(k)},\cdots,s_{\frac{M-1}{2},l0}^{(k)}\right]^{\mathrm{T}}$. In comparison with the range-compressed signal model given by Eq. (9), it is found that after the linear frequency-dependent phase compensation performed by $D_n(f)$, Eq. (33) gives a compact linear model for onboard real-time beamforming which has exactly the same form for the ground a posteriori DBF in Ref. [8]. This means the already well-developed DBF algorithms can be directly used here after some necessary modifications.

For instance, with a reasonable optimization criteria to keep the signal distortionless while simultaneously minimizing the response due to noise, using the Linear Constrained Minimum Variance (LCMV) method[7,8], one can derive the following real-time weight vector as

$$\begin{aligned} \boldsymbol{w}_{\mathrm{RT}}^{\mathrm{H}}(t) = \boldsymbol{w}_{\mathrm{DR}}^{\mathrm{H}}(t) &= \boldsymbol{g}_{\mathrm{DR}}^{\mathrm{H}}\left(\boldsymbol{A}^{(0)\mathrm{H}}(t)\boldsymbol{R}_{\eta}^{-1}(t)\boldsymbol{A}^{(0)}(t)\right)^{-1} \\ &\quad\cdot\boldsymbol{A}^{(0)\mathrm{H}}\boldsymbol{R}_{\eta}^{-1}(t) \end{aligned} \tag{34}$$

where $\boldsymbol{g}_{\mathrm{DR}}$ is the distortionless response constraint vector, and $\boldsymbol{R}_{\eta}(t)$ denotes the noise covariance matrix. Note that directional range ambiguities from other PRIs ($k\neq 0$) are ignored to simplify the real-time beamforming, and the noise is assumed to be white and complex normal distributed with zero mean and noise power $\sigma_{\mathrm{noise}}^2$. Then $\boldsymbol{w}_{\mathrm{RT}}^{\mathrm{H}}(t)$ can be shortened as its quiescent state form

$$\boldsymbol{w}_{\mathrm{RT}}^{\mathrm{H}}(t) = \boldsymbol{w}_{\mathrm{DR}}^{\mathrm{H}}(t) = \boldsymbol{g}_{\mathrm{DR}}^{\mathrm{H}}\left(\boldsymbol{A}^{(0)\mathrm{H}}(t)\boldsymbol{A}^{(0)}(t)\right)^{-1}\boldsymbol{A}^{(0)\mathrm{H}}(t) \tag{35}$$

It is easy to find that the weighting vector in Eq. (34) and Eq. (35) have almost same forms with the ones which are given in Refs. [7,8] derived with the same LCMV method. Nevertheless, it should be noted that there is still a major difference on the definition of the constraint vector $\boldsymbol{g}_{\mathrm{DR}}$. In this paper, $\boldsymbol{g}_{\mathrm{DR}}$ comprises M distortionless response constraints for each subpulse and should be denoted as $\boldsymbol{g}_{\mathrm{MDR}}$

$$\boldsymbol{g}_{\mathrm{MDR}} = [\ 1\quad 1\quad\cdots\quad 1\ ]_{1\times M}^{\mathrm{T}} \tag{36}$$

It is reasonable since here it is not the duty of the onboard DBF to do the echo separation, so

that no null is needed. However, in Refs. [7,8], $\boldsymbol{g}_{\mathrm{DR}}=\boldsymbol{e}_m=[0\ \cdots\ 0\ \ 1\ \ 0\ \cdots\ 0]^{\mathrm{T}}_{1\times M}$, it is defined as the mth column vector of the $M\times M$ identity matrix. In this case, M–1 nulls are formed to cancel M–1 echoes from the corresponding subpulses, only one subpulse echo is distortionless retained.

According to the relationship given by Eq. (A-5), $\boldsymbol{w}^{\mathrm{H}}_{\mathrm{MDR}}(t)$ can be further given by

$$\begin{aligned}\boldsymbol{w}^{\mathrm{H}}_{\mathrm{MDR}}(t) &= \left[\boldsymbol{g}^{\mathrm{H}}_{\mathrm{MDR}}\left(\bar{\boldsymbol{A}}^{(0)\mathrm{H}}\bar{\boldsymbol{A}}^{(0)}\right)^{-1}\bar{\boldsymbol{A}}^{(0)\mathrm{H}}\right]\boldsymbol{\Lambda}^{\mathrm{H}}(t)\\ &\triangleq \bar{\boldsymbol{w}}^{\mathrm{H}}_{\mathrm{MDR}}\boldsymbol{\Lambda}^{\mathrm{H}}(t)\end{aligned}\tag{37}$$

Just like what done in Section 3.2.1 and Appendix B, we can also derive a weighting vector to relax the distortionless demand but prefer SNR performance. In Appendix C such a SNR-prefer $\bar{\boldsymbol{w}}^{\mathrm{H}}_{\mathrm{MSNR}}$ is derived which can be an alternative of $\bar{\boldsymbol{w}}^{\mathrm{H}}_{\mathrm{MDR}}$ in Eq. (37).

One should note that the real-time weighting vectors Eq. (37) are normally configured in a deterministic manner onboard the satellite, so that $\boldsymbol{A}^{(0)}$ and $\boldsymbol{\Lambda}^{\mathrm{H}}(t)$ in Eq. (37) are predetermined based on an assumed earth model. The output signals $y_{\mathrm{sub}\_l}(t)$ from each subaperture are then given by

$$\begin{aligned}&y_{\mathrm{sub}\_l}(t)=\sum_{k=-\infty}^{\infty}s^{(k),\mathrm{out}}_{\mathrm{sub}\_l}(t)+\eta^{\mathrm{out}}_{\mathrm{sub}\_l}(t),\\ &\quad l=0,1,2,\cdots,L-1\end{aligned}\tag{38a}$$

$$\left.\begin{aligned}s^{(k),\mathrm{out}}_{\mathrm{sub}\_l}(t)&=\left[\boldsymbol{w}^{\mathrm{H}}_{\mathrm{RT}}(t)\boldsymbol{A}^{(k)}(t)\right]\boldsymbol{s}^{(k)}_{\mathrm{sub}\_l}(t)\\ &\triangleq \boldsymbol{q}^{(k)\mathrm{T}}_{\mathrm{RT}}\boldsymbol{s}^{(k)}_{\mathrm{sub}\_l}(t)\\ \boldsymbol{\eta}^{\mathrm{out}}_{\mathrm{sub}\_l}(t)&=\boldsymbol{w}^{\mathrm{H}}_{\mathrm{RT}}(t)\boldsymbol{\eta}_{\mathrm{sub}\_l}(t)\end{aligned}\right\}\tag{38b}$$

It is clear that $\boldsymbol{q}^{(k)}_{\mathrm{RT}}$ is made up of the final weighting coefficients for individual returns from multiple transmit subpulses. It is easy to know that letting $t\in\left[\tau^{\min}_{\mathrm{delay}},\tau^{\max}_{\mathrm{delay}}\right]$, $\boldsymbol{q}^{(0)}_{\mathrm{RT}}$ will correspond to desired signal return and $\boldsymbol{q}^{(k\neq 0)}_{\mathrm{RT}}$ to the kth ambiguity return. If ignoring the influence of model mismatch in the presence of topographic height variation, according to the definition of $\boldsymbol{w}^{\mathrm{H}}_{\mathrm{MDR}}(t)$ and $\boldsymbol{w}^{\mathrm{H}}_{\mathrm{MSNR}}(t)$, it is easy to derive that $\boldsymbol{q}^{(0)}_{\mathrm{RT}}$ for the distortionless response weighting $\boldsymbol{w}^{\mathrm{H}}_{\mathrm{RT}}=\boldsymbol{w}^{\mathrm{H}}_{\mathrm{MDR}}$ is

$$\boldsymbol{q}^{(0)\mathrm{T}}_{\mathrm{RT}}=\boldsymbol{g}^{\mathrm{H}}_{\mathrm{DR}}=[\ 1\quad 1\quad\cdots\quad 1\ ]_{1\times M}\tag{39}$$

which will ensure the distortionless responses, and for the maximized SNR weighting $\boldsymbol{w}^{\mathrm{H}}_{\mathrm{RT}}=\boldsymbol{w}^{\mathrm{H}}_{\mathrm{MSNR}}$, $\boldsymbol{q}^{(0)}_{\mathrm{RT}}$ now is

$$\boldsymbol{q}^{(0)\mathrm{T}}_{\mathrm{RT}}=\boldsymbol{c}^{\mathrm{H}}_{\max}\bar{\boldsymbol{A}}^{(0)\mathrm{H}}\bar{\boldsymbol{A}}^{(0)}\tag{40}$$

Since the elements in above $\boldsymbol{q}^{(0)\mathrm{T}}_{\mathrm{RT}}$ is normally unequal, a certain inter-subpulse relative distortion will occur as the price of maximizing SNR.

3.2.4 Analysis of realtime computational load

For the purpose of analyzing the realtime computational load of the proposed onboard DBF, the amount of real multiplications is derived in this subsection. It is known that the proposed realtime DBF approach in Section 3.2 is a deterministic DBF process. The fast-time-variant weighting vector in Eq. (23) is pre-determined and those weighting coefficients can be calculated in advance and stored in the onboard memory. However, since for each fast-time sample, a N-dimensional complex weighting vector is to be stored, a total huge onboard memory size is needed for the whole receive window. In order to save onboard memory, as a reasonable compromise, we can only calculate in advance $\bar{\boldsymbol{w}}^{\mathrm{H}}_{\mathrm{RT}}$ and $\boldsymbol{\Lambda}(t)$ in the time-variant weighting vector of Eq. (23), then for each fast-time sampling time, an additional computational load of N-point complex multiplications is essential.

Assuming Y fast-time samples in the receive echo window, the whole number of real multiplications of the present DBF processing for the Type-A beamforming given in Section 3.2.1 can be expressed as

$$T_1=Y\times N\times 3+Y\times L_0\times 3=Y\times N\times 3\times(L+1)\tag{41}$$

In Eq. (41), the first term after the equal sign represents the added real-time computation for N complex weighting coefficients calculation, where 3 real multiplications for realizing one complex multiplication is assumed[24].

In order to realize the Type-B beamforming scheme discussed in Section 3.2.3, it should be noted that besides the above additional computational load, now a FIR interpolation filtering for each antenna element channel is essential. Considering a P-order FIR interpolation filter is used in each antenna element channel, according to the ROP (Resource Occupation Reduced) processing

scheme given in Ref. [24], now the whole number of real multiplications of the Type-B DBF processing can be expressed as

$$\begin{aligned} T_2 &= Y \times L_0 \times (P+2) + Y \times N \times 3 + Y \times L_0 \times 3 \\ &= Y \times N \times [L \times (P+2) + 3(L+1)] \end{aligned} \tag{42}$$

As a reference level of onboard computational load, assuming with the same digital receiving structure of the DBF SAR and only employing the basic power combination among the multiple onboard channels toward a fixed direction in a digital way like the method given in Ref. [8], the number of real multiplications can be expressed as

$$T_0 = Y \times L_0 \times 3 = Y \times N \times 3 \times L \tag{43}$$

The comparison between T_1, T_2 and T_0 is illustrated in Fig. 4. The parameter values in the simulating is in accordance with the simulation given in Section 5. It can be seen that although the Type-A beamforming scheme implements an onboard time-variant beam scanning for SNR-Preserving, under the same output channel number, the additional realtime computational load is small in comparison with the present computational load level only implementing basic digital power combination toward fixed direction[8]. For the Type-B beamforming scheme, however, the added realtime computational load is sizable and should be considered in practical use.

3.3 Ground Reconstruction

3.3.1 Range focusing and the unified range-compressed signal form

Before signal reconstruction processing in elevation on the ground, data should be range focused first to minimize the pulse extension. Under the condition that the time-shifted chirped subpulse waveform scheme given in Eq. (3) is employed, a common match filter can be used for multiple transmit subpulses

$$h(t) = A_{\mathrm{c}} \cdot p_0^*(-t) \tag{44}$$

where $A_{\mathrm{c}} = \sqrt{|K_{\mathrm{r}}|}$ is a constant amplitude which keeps matched signal output energy unaltered. From Eq. (25) and Eq. (38), it is easily known that whether the Type-A beamformers derived in section 3.2.1, or the Type-B beamformers further exploring subpulse structure information in section 3.2.3 are used, the output signal corresponding to the echo of the mth subpulse in the kth PRI can be expressed by the following unified form for the lth subaperture

$$\begin{aligned} s_{m,\mathrm{sub}\_l}^{(k),\,\mathrm{out}}(t) = &\left\{ g_m^{(k)}(t - mT - kT_{\mathrm{r}}) \right. \\ &\left. \cdot \exp\left[\mathrm{j}2lN\pi f_{\mathrm{c}} \Delta\tau_m^{(k)}(t) \right] \right\} \otimes p_{\mathrm{rt},m}^{(k)}(t) \end{aligned} \tag{45}$$

where $p_{\mathrm{rt},m}^{(k)}(t)$ is the output reference pulse after real-time beamforming, for the Type-A case, according to Eq. (24) and Eq. (25), $p_{\mathrm{rt},m}^{(k)}(t)$ is denoted as $p_{\mathrm{rt\_A},m}^{(k)}(t)$ and expressed by

$$p_{\mathrm{rt\_A},m}^{(k)}(t) = \widehat{p}_{0,m}^{(k)}(t) = \mu_m^{(k)}(t) \cdot p_0(t) \tag{46}$$

and for the Type-B case, according to Eq. (38), $p_{\mathrm{rt},m}^{(k)}(t)$ is denoted as $p_{\mathrm{rt\_B},m}^{(k)}(t)$ and expressed by

$$p_{\mathrm{rt\_B},m}^{(k)}(t) = \left[\boldsymbol{q}_{\mathrm{RT}}^{(k)} \right]_m \cdot p_0(t) \tag{47}$$

Note that for a Type-A beamformer, there exists possible intra-subpulse distortion function $\mu_m^{(k)}(t)$ caused by the time-variant array pattern weighting, which may cause a degree of mismatching for the matched filtering Eq. (44). The matched filtering output of $s_{m,\mathrm{sub}\_l}^{(k),\,\mathrm{out}}(t)$, denoted as $\tilde{s}_{m,\mathrm{sub}\_l}^{(k)}(t)$, then can be uniformly represented by

$$\begin{aligned} \tilde{s}_{m,\mathrm{sub}\_l}^{(k)}(t) = &\left\{ g_m^{(k)}(t - mT - kT_{\mathrm{r}}) \right. \\ &\left. \cdot \exp\left[\mathrm{j}2lN\pi f_{\mathrm{c}} \Delta\tau_m^{(k)}(t) \right] \right\} \otimes p_{\mathrm{c},m}^{(k)}(t) \end{aligned} \tag{48}$$

where $p_{\mathrm{c},m}^{(k)}(t)$ is the range compressed version of $p_{\mathrm{rt},m}^{(k)}(t)$, which is for a Type-B beamformer

$$\begin{aligned} p_{\mathrm{c\_B},m}^{(k)}(t) &= p_{\mathrm{rt\_B},m}^{(k)}(t) \otimes h(t) \\ &= \left[\boldsymbol{q}_{\mathrm{RT}}^{(k)} \right]_m \cdot A_{\mathrm{c}} \cdot p_0(t) \otimes p_0^*(-t) \\ &\triangleq \left[\boldsymbol{q}_{\mathrm{RT}}^{(k)} \right]_m \cdot p_{\mathrm{comp}}(t) \end{aligned} \tag{49}$$

and for a Type-A beamformer

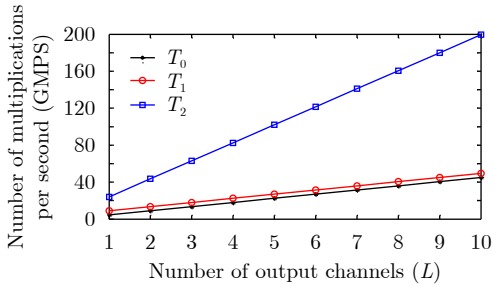

Fig. 4 Number of real multiplications per second of the proposed two types of onboard DBF processing and the reference beamforming processing given in Ref. [8] (N=5 and P= 8)

$$p_{\mathrm{c\_A},m}^{(k)}(t)=\widehat{p}_{0,m}^{(k)}(t)\otimes h(t)=A_{\mathrm{c}}\cdot\left[\mu_m^{(k)}(t)\cdot p_0(t)\right]\otimes p_0^*(-t)\approx q_m^{(k)}\cdot p_{\mathrm{comp}}(t) \tag{50}$$

In above two equations, $p_{\mathrm{comp}}(t)$ is a sinc-type function. Note that in Eq. (50) an approximation is made that the defocusing effect of mismatching caused by $\mu_m^{(k)}(t)$ is ignored and the peak gain decrease $q_m^{(k)}$ is concerned, which can be expressed as

$$q_m^{(k)}=\left[\frac{1}{T_{\mathrm{p}}}\int_{-\frac{T_{\mathrm{p}}}{2}}^{\frac{T_{\mathrm{p}}}{2}}\left|\mu_m^{(k)}(\xi)\right|^2\mathrm{d}\xi\right]^{\frac{1}{2}} \tag{51}$$

By comparing the Type-A version in Eq. (50) and the Type-B version in Eq. (49), it is clear that if we redefine the vector $\boldsymbol{q}_{\mathrm{RT}}^{(k)}$, whose mth element is equal to $q_m^{(k)}$, then we can unify the two type of beamforming signal models after range focusing, only keeping in mind that the real meaning of $\boldsymbol{q}_{\mathrm{RT}}^{(k)}$ is not the same. Using the same short-pulse-extent approximation which has been explained for Eq. (A-1), one can easily derive the following relation

$$\begin{aligned}\tilde{s}_{m,\mathrm{sub\_}l}^{(k)}(t)&=\exp\left[\mathrm{j}2lN\pi f_{\mathrm{c}}\Delta\tau_m^{(k)}(t)\right]\tilde{s}_{m,\mathrm{sub\_}0}^{(k)}(t)\\&\triangleq\exp\left[\mathrm{j}2lN\pi f_{\mathrm{c}}\Delta\tau_m^{(k)}(t)\right]\tilde{s}_m^{(k)}(t)\end{aligned} \tag{52}$$

then the full form of the output signals from the L channels of onboard Type-A or Type-B DBF network, *i.e.* $\tilde{\boldsymbol{y}}_{\mathrm{sub}}(t)=\left[\tilde{y}_{\mathrm{sub\_}0}(t),\cdots,\tilde{y}_{\mathrm{sub\_}l}(t),\cdots,\tilde{y}_{\mathrm{sub\_}L-1}(t)\right]^{\mathrm{T}}$ can be represented in matrix form as

$$\tilde{\boldsymbol{y}}_{\mathrm{sub}}(t)=\sum_{k=-\infty}^{\infty}\boldsymbol{V}^{(k)}(t)\left[\boldsymbol{q}_{\mathrm{RT}}^{(k)}\odot\tilde{\boldsymbol{s}}_{\mathrm{sub\_}0}^{(k)}(t)\right]+\tilde{\boldsymbol{\eta}}_{\mathrm{sub}}^{\mathrm{out}}(t) \tag{53a}$$

where $\tilde{\boldsymbol{s}}_{\mathrm{sub\_}0}^{(k)}(t)=\left[\tilde{s}_{-\frac{M-1}{2}}^{(k)}(t),\cdots,\tilde{s}_m^{(k)}(t),\cdots,\tilde{s}_{\frac{M-1}{2}}^{(k)}(t)\right]^{\mathrm{T}}$ is the reference-channel (the zero-th subaperture) echo vector comprising multiple transmit subpulses, $\odot$ denotes Hadamard product, and

$$\tilde{\boldsymbol{\eta}}_{\mathrm{sub}}^{\mathrm{out}}(t)=\left[\tilde{\eta}_{\mathrm{sub\_}0}^{\mathrm{out}}(t),\cdots,\tilde{\eta}_{\mathrm{sub\_}l}^{\mathrm{out}}(t),\cdots,\tilde{\eta}_{\mathrm{sub\_}L-1}^{\mathrm{out}}(t)\right]^{\mathrm{T}} \tag{53b}$$

$$\boldsymbol{V}^{(k)}(t)=\left[\begin{array}{ccccc}\boldsymbol{v}_{-\frac{M-1}{2}}^{(k)}(t)&\cdots&\boldsymbol{v}_m^{(k)}(t)&\cdots&\boldsymbol{v}_{\frac{M-1}{2}}^{(k)}(t)\end{array}\right] \tag{53c}$$

$$\boldsymbol{v}_m^{(k)}(t)=\left[\begin{array}{cccc}1&\mathrm{e}^{\mathrm{j}2N\pi f_{\mathrm{c}}\Delta\tau_m^{(k)}(t)}&\cdots&\mathrm{e}^{\mathrm{j}2(L-1)N\pi f_{\mathrm{c}}\Delta\tau_m^{(k)}(t)}\end{array}\right]^{\mathrm{T}} \tag{53d}$$

3.3.2 Ground reconstruction DBF algorithm

The linear signal model given by Eq. (53) will pose the following basic constraints on the ground weighting vectors to reconstruct the SAR returns from multiple transmit subpulses

$$\boldsymbol{w}_{\mathrm{g},m}^{\mathrm{H}}(t)\boldsymbol{V}^{(0)}(t)=\boldsymbol{e}_m^{\mathrm{H}} \tag{54}$$

$\boldsymbol{w}_{\mathrm{g},m}^{\mathrm{H}}(t)$ will restore the range compressed echo of the mth transmit subpulse without distortion, in the meantime cancel echoes of the other transmit subpulses, under the condition that accurate steering vectors in $\boldsymbol{V}^{(0)}(t)$ are available. However, in the presence of topographic height variations, merely fulfilling the predetermined constraint Eq. (54) will not ensure either sufficient interference suppression or signal gain, due to the deviation of the presupposed Direction Of Arrival (DOA) from the real one. Data-dependent adaptive methods can provide performance improvement, *e.g.*, by introducing signal covariance matrix estimation. Positions of nulls of the formed receive pattern can be selected adaptively to offer more reliable suppression to echoes from other transmit subpulses. However, the signal gain of the desired transmit subpulse is still sensitive to DOA errors and may not be protected well enough under a considerable DOA mismatch.

A widely used robust DBF technique which offers better protection for desired signal gain under DOA mismatch is diagonal loading, which will work well if interferences are much stronger than the desired signal[26]. However, it is obvious from Eq. (54) that 'interference' and 'signal' are interchangeable. Echoes from different transmit subpulses are with similar power level, at this point diagonal loading is not quite a suitable solution. Other methods to enhance the DBF robustness against the DOA mismatch include imposing additional derivative constraints[26], covariance matrix tapering technique[27] and so on. These methods can offer wider response at the look angle corresponding to the desired transmit subpulse, or even widened nulls for interferences from other transmit subpulses. However, one has to devote much more additional system DOFs, it means here that the onboard output channel number L

should be much larger than the subpulse number M. This condition obviously goes against the original intention to minimize onboard output channels.

In summary, the ground reconstruction based on the signal model Eq. (53) has the characteristics as follows: (1) the signal-plus-interference number M is known in advance (returns from other PRIs or layover sources are omitted); (2) a comparatively high and stable signal/interference power level relative to noise is predictable, considering the demanding SAR application requirement; (3) only a limited system DOFs are offered, due to the data downlink rate limit.

According to above characteristics, a two-step strategy is considered here. First, a DOA-estimation preprocessing step is introduced for the known number of transmit subpulses based on the range compressed array data, which can significantly reduce the source DOA uncertainty, owing to the high and stable signal/interference power level relative to noise. Then, Eigen-Space based method is employed to improve robustness: each steering vector (column vectors of $\boldsymbol{V}^{(0)}$), after renewed with the estimated DOA, is projected to the estimated signal-plus-interference subspace obtained via the eigen-decomposition of the sample covariance matrix, in order to further reduce steering vector errors caused by the residual DOA errors.

Supposing that using a direction-finding algorithm like Root-MUSIC[26], look angels of M returns are estimated and $\hat{\boldsymbol{V}}^{(0)}(t)$ is calculated according to Eq. (53c), in the meantime $\hat{\boldsymbol{R}}_{\tilde{y}} = \boldsymbol{U}_{\mathrm{sI}}\Sigma_{\mathrm{sI}}\boldsymbol{U}_{\mathrm{sI}}^{\mathrm{H}}$ is obtained by the eigenvalue decomposition of $\hat{\boldsymbol{R}}_{\tilde{\boldsymbol{y}}}$, which is the estimated covariance matrix of $\tilde{\boldsymbol{y}}_{\mathrm{sub}}(t)$, where Σ_{sI} is the diagonal matrix comprising M principal eigenvalues of $\hat{\boldsymbol{R}}_{\tilde{\boldsymbol{y}}}$, $\boldsymbol{U}_{\mathrm{sI}}$ is the signal-plus-interference subspace matrix comprising M principal eigenvectors. Then the modified constraint matrix after the signal-plus-interference subspace orthogonal projection is

$$\widehat{\boldsymbol{V}}^{(0)} = \boldsymbol{U}_{\mathrm{sI}}\boldsymbol{U}_{\mathrm{sI}}^{\mathrm{H}}\hat{\boldsymbol{V}}^{(0)} \tag{55}$$

Then the optimum beamformer maintaining distortionless response to the desired signal while minimizing the output interference-plus-noise power can be represented by

$$\begin{aligned}\boldsymbol{w}_{\mathrm{g},m}^{\mathrm{H}} = \boldsymbol{w}_{\mathrm{g\_opt},m}^{\mathrm{H}} &= \boldsymbol{e}_m^{\mathrm{H}}\left[\widehat{\boldsymbol{V}}^{(0)\mathrm{H}}\hat{\boldsymbol{R}}_{\tilde{y}}^{-1}\widehat{\boldsymbol{V}}^{(0)}\right]^{-1}\widehat{\boldsymbol{V}}^{(0)\mathrm{H}}\hat{\boldsymbol{R}}_{\tilde{y}}^{-1}\\ &= \boldsymbol{e}_m^{\mathrm{H}}\left[\hat{\boldsymbol{V}}^{(0)\mathrm{H}}\boldsymbol{U}_{\mathrm{sI}}\boldsymbol{S}_{\mathrm{sI}}^{-1}\boldsymbol{U}_{\mathrm{sI}}^{\mathrm{H}}\hat{\boldsymbol{V}}^{(0)}\right]^{-1}\\ &\quad\cdot\hat{\boldsymbol{V}}^{(0)\mathrm{H}}\boldsymbol{U}_{\mathrm{sI}}\boldsymbol{S}_{\mathrm{sI}}^{-1}\boldsymbol{U}_{\mathrm{sI}}^{\mathrm{H}}\end{aligned} \tag{56}$$

It is clearly that $\boldsymbol{w}_{\mathrm{g\_opt},m}$ is within the signal-plus-interference subspace spanned by $\boldsymbol{U}_{\mathrm{sI}}$, which is the same subspace spanned by $\boldsymbol{V}^{(0)}$. If defining the following orthogonal projection matrix

$$\boldsymbol{P}_{\boldsymbol{v}} = \boldsymbol{V}^{(0)}\left[\boldsymbol{V}^{(0)\mathrm{H}}\boldsymbol{V}^{(0)}\right]^{-1}\boldsymbol{V}^{(0)\mathrm{H}} \tag{57}$$

the orthogonal projected version of $\boldsymbol{w}_{\mathrm{g\_opt},m}$ on the signal-plus-interference subspace is given by

$$\begin{aligned}\boldsymbol{w}_{\mathrm{g\_opt},m}^{\mathrm{H}} &= \boldsymbol{w}_{\mathrm{g\_opt},m}^{\mathrm{H}}\boldsymbol{P}_{\boldsymbol{v}}\\ &= \boldsymbol{e}_m^{\mathrm{H}}\left\{\left[\hat{\boldsymbol{V}}^{(0)\mathrm{H}}\boldsymbol{U}_{\mathrm{sI}}\boldsymbol{S}_{\mathrm{sI}}^{-1}\boldsymbol{U}_{\mathrm{sI}}^{\mathrm{H}}\hat{\boldsymbol{V}}^{(0)}\right]^{-1}\right.\\ &\quad\left.\cdot\hat{\boldsymbol{V}}^{(0)\mathrm{H}}\boldsymbol{U}_{\mathrm{sI}}\boldsymbol{S}_{\mathrm{sI}}^{-1}\boldsymbol{U}_{\mathrm{sI}}^{\mathrm{H}}\boldsymbol{V}^{(0)}\right\}\\ &\quad\cdot\left[\boldsymbol{V}^{(0)\mathrm{H}}\boldsymbol{V}^{(0)}\right]^{-1}\boldsymbol{V}^{(0)\mathrm{H}}\end{aligned} \tag{58}$$

Under the condition that the estimation of $\boldsymbol{V}^{(0)}$ is enough accurate, ignoring the difference between $\hat{\boldsymbol{V}}^{(0)}$ and $\boldsymbol{V}^{(0)}$ in the brace of Eq. (58) yields

$$\boldsymbol{w}_{\mathrm{g\_opt},m}^{\mathrm{H}} \approx \boldsymbol{w}_{\mathrm{g\_q},m}^{\mathrm{H}} = \boldsymbol{e}_m^{\mathrm{H}}\left[\boldsymbol{V}^{(0)\mathrm{H}}\boldsymbol{V}^{(0)}\right]^{-1}\boldsymbol{V}^{(0)\mathrm{H}} \tag{59}$$

It is obvious that the derived $\boldsymbol{w}_{\mathrm{g\_q},m}^{\mathrm{H}}$ is in form the optimal quiescent weight vector of the well-known LCMV (linear constraints minimum variance) beamformer subject to the constraints of Eq. (54). It is also the analytical least square solution[8,26] subject to Eq. (54).

4 Uniform Performance Analysis

Since a unified range-compressed signal model and ground signal reconstruction DBF algorithm can be established in Section 3.3, an uniform performance analysis can be given. According to Eq. (53), echo from the mth transmit subpulse is separated unambiguously by $\boldsymbol{w}_{\mathrm{g},m}$ and can be written as

$$\begin{aligned}\tilde{s}_m^{\text{out}}(t) &= \boldsymbol{w}_{\text{g},m}^{\text{H}}\tilde{\boldsymbol{y}}_{\text{sub}}(t)\\ &= \underbrace{\boldsymbol{w}_{\text{g},m}^{\text{H}}\boldsymbol{V}^{(0)}\left(\boldsymbol{q}_{\text{RT}}^{(0)}\odot\boldsymbol{e}_m\right)\tilde{s}_m^{(0)}(t)}_{\text{signal}}\\ &\quad+\underbrace{\boldsymbol{w}_{\text{g},m}^{\text{H}}\boldsymbol{V}^{(0)}\sum_{m'=-\frac{M-1}{2},m'\neq m}^{\frac{M-1}{2}}\left(\boldsymbol{q}_{\text{RT}}^{(0)}\odot\boldsymbol{e}_{m'}\right)\tilde{s}_{m'}^{(0)}(t)}_{\text{residual interferences}}\\ &\quad+\underbrace{\sum_{k=-K_{\text{H}},k\neq0}^{K_{\text{H}}}\boldsymbol{w}_{\text{g},m}^{\text{H}}\boldsymbol{V}^{(k)}\left[\boldsymbol{q}_{\text{RT}}^{(k)}\odot\tilde{\boldsymbol{s}}_{\text{sub\_}0}^{(k)}(t)\right]}_{\text{ambiguities}}\\ &\quad+\underbrace{\boldsymbol{w}_{\text{g},m}^{\text{H}}\tilde{\boldsymbol{\eta}}_{\text{sub}}^{\text{out}}(t)}_{\text{receiver noise}}\end{aligned}\tag{60}$$

where K_{H} denotes the maximum range ambiguity number in consideration. The first term in Eq. (60) represents the unambiguously reconstructed returned signal from the mth transmit subpulse, the corresponding signal power $p_{\text{sig},m}(t)$ is

$$p_{\text{sig},m}(t)=\left|\left[\boldsymbol{q}_{\text{rt}}^{(0)}\right]_m\right|^2\cdot\left|\boldsymbol{w}_{\text{g},m}^{\text{H}}\boldsymbol{V}^{(0)}\boldsymbol{e}_m\right|^2\tilde{\sigma}_m^{2(0)}(t)\tag{61}$$

where $\tilde{\sigma}_m^{2(k)}(t)$ is the range compressed signal self-correlation derived in Appendix D and its expression is given by Eq. (D-6).

The second and the third term in Eq. (60) represent respectively the ambiguous components inside or outside the PRI, corresponding to residual interferences from other subpulses transmitted in the same PRI due to nonideal suppression, or ordinary sidelobe range ambiguity weighted by DBF network. According to the results in Appendix D, the total power of these ambiguous components is given by

$$\begin{aligned}p_{\text{amb},m}(t)=&\boldsymbol{w}_{\text{g},m}^{\text{H}}\left(\sum_{k=-K_{\text{H}}}^{K_{\text{H}}}\boldsymbol{V}^{(k)}\boldsymbol{\Gamma}_{\boldsymbol{q}}^{(k)}\boldsymbol{R}_{\tilde{\boldsymbol{s}}}^{(k)}\boldsymbol{\Gamma}_{\boldsymbol{q}}^{(k)\text{H}}\boldsymbol{V}^{(k)\text{H}}\right)\\ &\cdot\boldsymbol{w}_{\text{g},m}-p_{\text{sig},m}(t)\end{aligned}\tag{62a}$$

$$\begin{aligned}\boldsymbol{R}_{\tilde{\boldsymbol{s}}}^{(k)}(t)&=E\left[\tilde{\boldsymbol{s}}_{\text{sub\_}0}^{(k)}(t)\tilde{\boldsymbol{s}}_{\text{sub\_}0}^{(k)\text{H}}(t)\right]\\ &=\text{diag}\left\{\left[\tilde{\sigma}^{2(k)}_{-\frac{M-1}{2}}(t),\cdots,\tilde{\sigma}_m^{2(k)}(t),\cdots,\right.\right.\\ &\quad\left.\left.\tilde{\sigma}^{2(k)}_{\frac{M-1}{2}}(t)\right]\right\}\end{aligned}\tag{62b}$$

$$\boldsymbol{\Gamma}_{\boldsymbol{q}}^{(k)}=\text{diag}\left(\boldsymbol{q}_{\text{RT}}^{(k)}\right)\tag{62c}$$

The RASR corresponding to the mth transmit subpulse (also the mth azimuth subbeam for the multi-beam mode) is therefore evaluated by

$$\text{RASR}_m(t)=\frac{p_{\text{amb},m}(t)}{p_{\text{sig},m}(t)},\quad\tau_{\text{delay}}^{\min}\le t-mT\le\tau_{\text{delay}}^{\max}\tag{63}$$

Under the approximation that each transmit subpulse contributes the almost same signal power[8], the systemic RSAR for delay $\tau\in\left[\tau_{\text{delay}}^{\min},\tau_{\text{delay}}^{\max}\right]$ can be further evaluated by

$$\begin{aligned}\text{RASR}_{\text{sys}}(\tau)=&\frac{\sum_{m=-\frac{M-1}{2}}^{\frac{M-1}{2}}\text{RASR}_m(\tau+mT)}{M},\\ &\tau_{\text{delay}}^{\min}\le\tau\le\tau_{\text{delay}}^{\max}\end{aligned}\tag{64}$$

The last term in Eq. (60) represents the ultimate output noise from the cascaded DBF networks, which is the weighted sum of L noise components $\tilde{\eta}_{\text{sub\_}l}^{\text{out}}(t)$, $l=0,1,\cdots,L-1$. Under the approximation that the noise bandwidth is equal to the signal bandwidth, taking account that $h(t)$ is an ideal Passive Power Filter (PPF), it is easily derived that the noise power of $\tilde{\eta}_{\text{sub\_}l}^{\text{out}}(t)$ is given by

$$E\left[\left|\tilde{\eta}_{\text{sub\_}l}^{\text{out}}(t)\right|^2\right]=\sigma_{\text{noise}}^2\bar{\boldsymbol{w}}_{\text{RT}}^{\text{H}}\bar{\boldsymbol{w}}_{\text{RT}}\tag{65}$$

where σ_{noise}^2 is the noise power of each antenna element. The ultimate output noise power of the mth transmit subpulse is

$$\begin{aligned}p_{\text{noise},m}(t)&=E\left[\left|\boldsymbol{w}_{\text{g},m}^{\text{H}}\tilde{\boldsymbol{\eta}}_{\text{sub}}^{\text{out}}(t)\right|^2\right]\\ &=\sigma_{\text{noise}}^2\bar{\boldsymbol{w}}_{\text{RT}}^{\text{H}}\bar{\boldsymbol{w}}_{\text{RT}}\boldsymbol{w}_{\text{g},m}^{\text{H}}(t)\boldsymbol{w}_{\text{g},m}(t)\end{aligned}\tag{66}$$

The local SNR scaling by the cascaded DBF Networks in elevation corresponding to the mth subpulse is therefore evaluated by

$$\begin{aligned}\left(\frac{\text{SNR}_{\text{in}}}{\text{SNR}_{\text{out}}}\right)_{m\text{th}}&=\frac{\sigma_m^{2(0)}(t)/\sigma_{\text{noise}}^2}{p_{\text{sig},m}(t)/p_{\text{noise},m}(t)}\\ &=\frac{\sigma_m^{2(0)}}{\tilde{\sigma}_m^{2(0)}}\times\frac{\bar{\boldsymbol{w}}_{\text{RT}}^{\text{H}}\bar{\boldsymbol{w}}_{\text{RT}}}{\left|\left[\boldsymbol{q}_{\text{rt}}^{(0)}\right]_m\right|^2}\\ &\quad\times\frac{\boldsymbol{w}_{\text{g},m}^{\text{H}}(t)\boldsymbol{w}_{\text{g},m}(t)}{\left|\boldsymbol{w}_{\text{g},m}^{\text{H}}(t)\boldsymbol{V}^{(0)}(t)\boldsymbol{e}_m\right|^2}\\ &\approx\phi_{\text{rt},m}^r\phi_{\text{g},m}^r(t)\end{aligned}\tag{67}$$

where $\phi_{\text{rt},m}^r$ and $\phi_{\text{g},m}^r$ represent respectively the

SNR scaling caused by the onboard real-time DBF and a posteriori DBF on the ground. Note that here the approximation of $\tilde{\sigma}_m^{2(0)} \approx \sigma_m^{2(0)}$ is used (cf. (Eq. D-6) in Appendix). Under the approximation that each transmit subpulse contributes the same signal power[8], the systemic SNR scaling factor in elevation for delay $\tau \in \left[\tau_{\text{delay}}^{\min}, \tau_{\text{delay}}^{\max}\right]$ can be evaluated by

$$\Phi_{\text{bf}}^{r}(\tau) = \sum_{m=-\frac{M-1}{2}}^{\frac{M-1}{2}} \left[\phi_{\text{rt},m}^{r}\phi_{\text{g},m}^{r}(\tau + mT)\right]/M \tag{68}$$

It is easily understood from its definition that $\Phi_{\text{bf}}^{r}(\tau)$ has an optimum minimum value $1/L_0$, which means that the DBF network has oriented its maximum array gain toward the desired signal[8]. Also, it should be noted that $\Phi_{\text{bf}}^{r}(\tau)$ is a scaling factor of the output SNR relative to the input element-level SNR due to the DBF-network, therefore the effect of the element-level antenna gain changing in response to the element size d_0 to the ultimate output SNR is not counted. Supposing that the total receive antenna height H_{ant} has been predetermined to meet the requirement[4,8] for a reliable separation of multiple subpulses, then with the known condition $H_{\text{ant}} = d_0 \times L_0$, the output system SNR for a DBF network different antenna element size, *i.e.*, d_0 and d_0', is given by

$$\begin{aligned}\frac{\text{SNR}_{\text{out},d_0}}{\text{SNR}_{\text{out},d_0'}} &= \frac{d_0}{d_0'}\frac{G_{d_0,\text{drop}}(\beta)}{G_{d_0',\text{drop}}(\beta)}\frac{\Phi_{\text{bf},d_0'}^{r}}{\Phi_{\text{bf},d_0}^{r}} \\ &= \left[\frac{G_{d_0,\text{drop}}(\beta)}{L_0\Phi_{\text{bf},d_0}^{r}}\right] \Big/ \left[\frac{G_{d_0',\text{drop}}(\beta)}{L_0'\Phi_{\text{bf},d_0'}^{r}}\right]\end{aligned} \tag{69}$$

where $G_{d_0,\text{drop}}(\beta) = \text{sinc}^2\left[\pi d_0 \sin(\beta)/\lambda\right]$ represents the relative gain drop of a receive antenna element with the size d_0, which approaches the flat 0 dB in the illuminated swath if d_0 is small. When d_0' is small enough, in the most ideal case, $G_{d_0',\text{drop}}(\beta) \approx 1$ and $L_0'\Phi_{\text{bf},d_0'}^{r} = 1$, therefore, the ultimate SNR loss for a DBF network with the antenna element L_0(with element size d_0) relative to the optimal SNR output can be given by

$$L_r(\tau) = \frac{G_{d_0,\text{drop}}\left[\beta(\tau)\right]}{L_0}\left[\Phi_{\text{bf},d_0}^{r}(\tau)\right]^{-1} \tag{70}$$

Note that the value $L_{\text{r}}^{-1}(\tau) = [L_0/G_{d_0,\text{drop}}(\tau)]$ $\Phi_{\text{bf},d_0}^{r}(\tau)$ can be viewed as a normalized version of the systemic SNR scaling factor $\Phi_{\text{bf}}^{r}(\tau)$ to provide a fair comparison between various DBF networks with different structures. Also note that the optimum level of $L_{\text{r}}(\tau)$ is 0 dB.

5 Design Example and Simulation Results

In Ref. [8], it has been demonstrated by simulations that under the DOA mismatch condition, the underground a posteriori process employing adaptive beamforming is promising to provide much better performance compared with the real-time deterministic DBF[7], however, a more than double onboard channels and data downlink rate are required as the cost.

This paper, as a continuation, will mainly illustrate the achievable performance improvement of the cascaded hybrid DBF networks by making a direct comparison with the a posteriori DBF in Ref. [8] under the same MWE SAR mode employing multiple azimuth subbeams on transmit. Therefore, we consider a design example of an X-band spaceborne SAR with an azimuth resolution of 1.5 m and a swath width of 100 km, which has the same essential parameters (summarized in Tab. 1) as the exemplary system simulated in Ref. [8]. A transmit signal with M=4 chirped subpulses is assumed, each subpulse has a bandwidth of 250 MHz and a duration of 40 μs, and is mutually time shifted[4], the interval time between adjacent subpulses is also 40 μs. The transmit signal scheme is same with that given in Ref. [8]. The antenna height is properly designed and equal to 2.33 m, which meets the subpulse-separation requirement on the antenna height given by the Eq. (28) in Ref. [8]. The timing diagram of the exemplary system can be found in Fig. 2 of Ref. [8].

The only difference is the onboard output data channel number L, which is equal to the number of the subapertures in elevation. In Ref. [8] $L = L_0$, and its value is variable and tested from 5, 6, 10 up to 150. It is pointed out in Ref. [8] that since no onboard realtime DBF network is employed, the channel number L is restricted by four inherent constraints, these constraints include the reliable signal separation constrain, the swath-bor-

Tab. 1 Parameters used in the system simulation[8]

Parameter	Value	Parameter	Value
Wave length	0.031 m	Number of subpulses	4
Swath width	100 km	PRF	1310 Hz
Off-nadir angle	18°～24°	Azimuth subapertures	4
Azimuth resolution	1.5 m	Antenna length	10.8 m
Band width	250 MHz	Antenna height	2.33 m
Ground range resolution at center	1.5 m	Processed Doppler bandwidth	4890 Hz
Onboard elevation channel number	6	Azimuth ambiguity to signal ratio	–30 dB
Orbital altitude	800 km	Subpulse duration/ interval	40 μs

der gain-drop constrain, pulse-interval efficient utilization constrain, and the DOF constrain[8]. In order to satisfy the multiple constrains, a channel number L=10, which is 2.5 times of the transmit subpulse number (*i.e.* M=4), is required, especially for avoiding significant signal gain loss at swath borders. In this paper, however, owing to the employment of the onboard real-time scanning DBF network, the original swath-border gain-drop restrict is relaxed. A channel number L=6, which is only slightly larger than the transmit subpulse number, is selected and demonstrated in the following simulation.

In azimuth dimension, under the selected PRF=1310 and the processed Doppler bandwidth of 4890 Hz, with four azimuth subapertures, the azimuth ASR after intra-subbeam azimuth spectrum reconstruction and inter-subbeam spectrum combination is approximate –30 dB, according to the azimuth-dimensional reconstruction algorithms given in Refs. [3,6]. The following simulations will be focused on the performance in elevation dimension only.

In the following simulations, the true topographic heights of the imaged scene are deliberately set with a deviation of $\Delta h = 250$ m relative to the given default earth model. Though it was found in Ref. [23] that the main-beam gain and SNR loss caused by such a height deviation is neglectable for the SCORE deterministic beamforming in a DBF-SAR system, the RASR degradation for the deterministic ANS DBF in a MWE-SAR system is already unacceptable[8].

At the first stage of the simulation, for the purpose of providing explicit and quick assessing the achievable best performance for the presented hybrid DBF networks in comparison with the a posteriori DBF in Ref. [8], a standard array is assumed, and also assumed is that in both cases the DOA mismatch can be accurately handled by the ground DOA-estimation and robust beamforming in the ground. By setting $d_0 = \lambda/2$, there are $L_0 = 150$ antenna elements in elevation constituting the full aperture with the height of 2.33 m. For the ground part DBF network, since the data-dependent adaptive beamformer given by Eq. (56) will very close to its quiescent form if accurate DOA information is available, we will directly employ the optimal quiescent LCMV weighting vector given by Eq. (59) with true DOA to avoid the uncertainty caused by data-dependent algorithm. For the a posteriori DBF, $L = L_0 = 6$ is directly set, and the same quiescent LCMV weighting vector is also used for the sake of fairness. On the satellite, for the onboard DBF network, weighting vectors are calculated with the deterministic DOA information according to the default earth model.

The cascaded hybrid DBF networks employing onboard Type-A beamforming presented in Section 3.2.1 are investigated first. The array patterns of the distortionless-preferred ESLC beamformer and the SNR-preferred DPSS beamformer are shown in Fig. 5 for $t = \tau_c$. The two weighting vectors are power normalized to the power level of $\bar{\boldsymbol{w}}_{\mathrm{ESLC}}$ to keep the same output noise power level. Over the extent of each transmit subpulse, there is a corresponding variant array gain weighting function. Therefore, as shown in Fig. 5, each subpulse extend is mapped into a given segment on the abscissa axis, which is indicated by a vertical bar. The amplitude variation in the extent of each subpulse will cause the intra-subpulse distortion and can be represented by the function $\mu_m^{(k)}(t)$ according to Eq. (26). In Fig. 6, the different distortion functions $\mu_m^{(0)}(t)$ for mul-

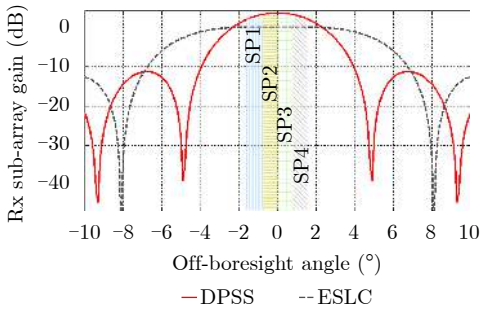

Fig. 5 The array patterns of onboard Type-A beamforming at instantaneous time $t = \tau_c$

tiple subpulses are simulated and shown for the distortionless-preferred ESLC and the SNR-preferred DPSS beamformer, with gray line and red line respectively.

It is shown in Fig. 5 that indeed the distortionless-preferred ESLC beamformer can output a nearly constant gain for each subpulse. From the enlarged view in Fig. 6(b), the distortion functions $\mu_m^{(0)}(t)$ for the four subpulses are flat enough with only a ± 1.2 dB of gain variation. However, it is obvious that the distortionless response is achieved at the price of considerable array gain loss. The SNR-preferred DPSS beamformer, on the contrary, can get higher signal gains with mild inter- and intra-subpulse distortion. With the given system parameters in the present example, by maximizing the antenna directivity on the entire instantaneous scattering angular region, the DPSS beamforming gets an array pattern which has a main-beam shape similar to that of the normal beamformer, but with a lower side-lob level implying a more powerful ambiguity-suppression ability. The 3 dB-mainbeam width is slightly wider than the angular region covering the entire instantaneous scattering field containing 4 subpulses. From Fig. 6(a), it is shown the distortion functions $\mu_m^{(0)}(t)$ for the four subpulses are within an acceptable ± 1.2 dB of gain variation. The form of $\mu_m^{(0)}(t)$ is known and can be compensated in the processing.

In Fig. 7, performance comparison on RASR between the hybrid Type-A DBF networks and the a posteriori DBF[8] is provided, with the same onboard data channel number ($L = 6$) and same antenna height. It is found that with the DPSS hybrid DBF networks, either the swath average value (–49.3 dB) or the worst case value (–38.1 dB) of RASR is much better than that of the ground DBF (–47.1 dB for average and –30.4 dB the worst), due to its time-variant weighting fulfilling optimization of the overall signal power over the whole swath. With the ESLC hybrid DBF networks, considering its signal gain loss for the sake of keeping distortionless response, the RASR values in average (–35.4 dB), though quite acceptable, are not as good as the ground DBF, however, at swath borders, the worst case value (–34.9 dB) is still much better. Normally the worst case maximum RASR is a key indicator for performance evaluation.

The corresponding SNR performance comparison, *i.e.* the normalized total SNR loss $L_r(\tau)$ further counting the effect of the element-level antenna gain variation, is given in Fig. 8. It is shown that the performance of the cascaded hybrid DBF structures on the total SNR loss $L_r(\tau)$ relative to the achievable optimum SNR is much better and evenly distributed in the whole swath than that of the ground DBF, especially at the swath borders, there is 6.6 dB SNR improvement for DPSS hybrid networks and about 3.6 dB improvement for that of ESLC. From this point, the SNR-preferred DPSS is recommendable. At the swath center, the value of $L_r(\tau)$ is slightly better

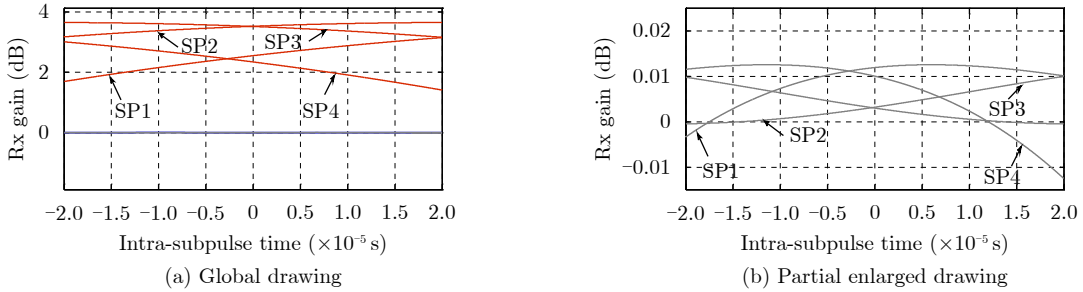

(a) Global drawing (b) Partial enlarged drawing

Fig. 6 Amplitude of the distortion functions $\mu_m^{(0)}(t)$ in the extent of each of 4 subpulses

for the ground DBF, it is reasonable, since for a staring illumination of each subaperture oriented to the swath center, a target at the swath center will get a invariable peak receive gain for each transmit subpulse in each subaperture.

From the Fig. 3 in Ref. [8], it is found that with as many as 10 channels using the ground DBF, the swath-average RASR value is about –51 dB and the worst-case value is about –40 dB, at the meantime, the SNR drop is about 2.5 dB at swath border in Fig. 4 of Ref. [8]. Compared with the results in Fig. 7 and Fig. 8, it is easily found that by employing the onboard time-variant beamforming, with 6 onboard output channels, the cascaded hybrid DBF networks can achieve satisfactory performance on range ambiguity suppression which approximates that of the ground DBF with as many as 10 channels, and even have more excellent performance on SNR preserving at swath borders.

Next, the Type-B hybrid DBF networks in Section 3.2.3 further exploring subpulse time-frequency structure information are investigated in a similar way. The array spatial patterns of the onboard LCMV-MDR beamformer and MSNR beamformer at time $t=\tau_c$ on carrier frequency are shown in Fig. 9. It should be noted that due to the linear frequency-dependent phase shifts introduced to signal paths within each subaperture prior to the followed weighted summation, echoes of the multiple transmit subpulses are given theoretically individual frequency-invariant gains, notwithstanding the uncompressed pulse extension and the time-variant array weighting. Therefore as shown in Fig. 9, each subpulse can be mapped into a given point on the abscissa axis, which is indicated by a vertical dashed line, not a vertical bar in Fig. 5 as a contrast. However, though in theory each subpulse can get a constant gain without PEL, it is not true that all subpulses can get the maximum peak gain of the array pattern just like the single-chirped-pulse case employing SCORE technique[15], due to the more complex inter-pulse chirped-subpulse structure.

In Fig. 10 and Fig. 11, performance comparisons on RASR and SNR between the hybrid Type-B DBF networks and the a posteriori DBF[8] are given, respectively. It is interesting to find much likeness between the results of Type-B DBF (Fig. 10, Fig. 11) and Type-A DBF (Fig. 7, Fig. 8). So it is essential to give an across comparison between the onboard signal-structure-dependent beamformers (Type-B) and the non-signal-dependent ones (Type-A). For both types, according to the

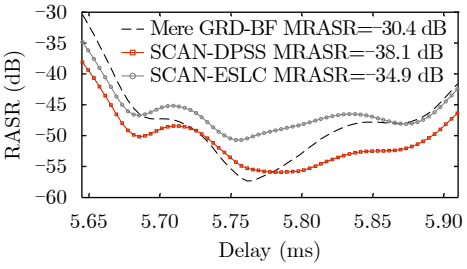

Fig. 7 Performance comparison on RASR between the cascaded hybrid Type-A DBF networks and ground DBF in Ref. [8]

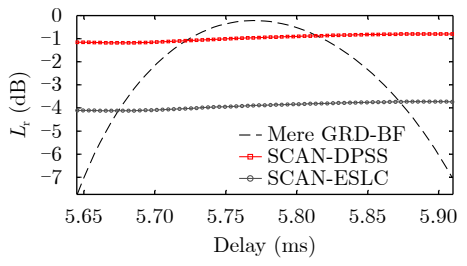

Fig. 8 Performance comparison on SNR between the cascaded hybrid Type-A DBF networks and ground DBF in Ref. [8]

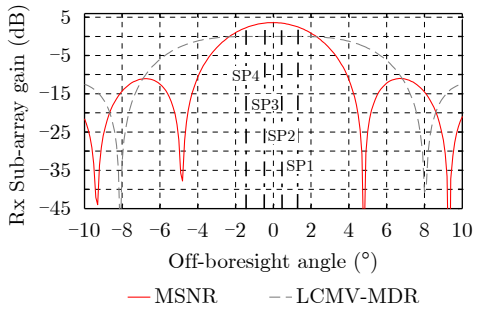

Fig. 9 The array patterns of onboard Type-B beamforming at instantaneous time $t=\tau_c$

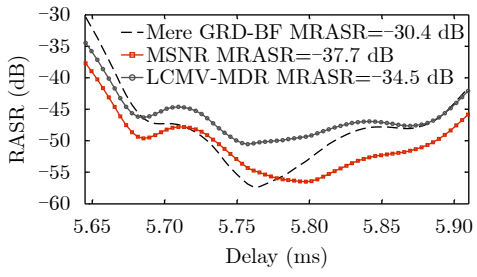

Fig. 10 Performance comparison on RASR between the cascaded hybrid Type-B DBF networks and ground DBF in Ref. [8]

given optimization objectives, there are two categories of beamformers: SNR-preserving-preferred category (DPSS in Type-A, MSNR in Type-B) and distortionless-response-preferred category (ESLC in Type-A, LCMV-MDR in Type-B). Comparison results of these two categories are given in Fig. 12. From Fig 12(a), it is found that with regard to the performance on RASR, there is no significant difference found if the transmit signal-structure information is used or not, either for SNR-preserving-preferred or distortionless-response-preferred category. With regard to the performance on SNR, however, there is a quite small advantage if the transmit signal-structure information is used, either for SNR-preserving-preferred or distortionless-response-preferred category. There are two aspects to explain why there is no remarkable advantage when prior information of the chirped subpulse time-frequency structure is utilized. The first aspect is that four-subpulses structure is complex enough, which prohibits all subpulses sharing the maximum peak gain of the array pattern like the SCORE case[22]; The second aspect is that the total and subaperture height is properly designed according to the multiple inherent constraints given in Ref. [8].

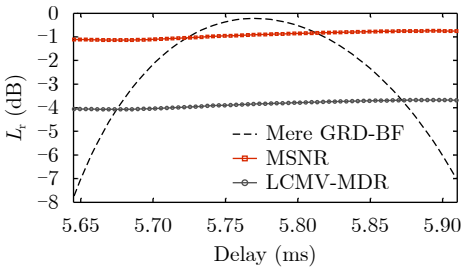

Fig. 11 Performance comparison on SNR between the cascaded hybrid Type-B DBF networks and ground DBF in Ref. [8]

At the second simulation stage, more practical considerations are included. First, the practical case when the antenna element spacing is larger than half of the wavelength is considered. The number of antenna element in elevation is reduced to 30, accordingly the antenna element spacing is increased to $d_0 = 2.5\lambda$. With the new element spacing, the performance on RASR and SNR for the Type-A DPSS and Type-B MSNR beamformers are shown in Fig. 13, both of which are SNR preferred. It's found that the RASR values near the swath center deteriorate in some degree with the much larger element size, however, the deterioration of the average RASR in the whole swath or the worst RASR in the swath border is not significant. With regard to the performance on SNR, since the total SNR loss $L_r(\tau)$ has accounted for the array element pattern, with a larger element size, there are inevitable deterioration at swath borders. In the given situation, the maximum deterioration is about 0.2 dB, which is acceptable under many circumstances.

Next, besides the more practical elements size, the DOA mismatch condition in the presence of non-negligible topographic height error is further investigated. This time, a performance comparison between the cascaded hybrid DBF networks and the onboard real-time null-steering DBF[7] is given under the above condition. The echoes received by $L_0 = 30$ elevation antenna elements, with additive thermal noise (Array SNR= 5 dB, cf. Refs. [23,26]) are simulated in accordance with the signal model given by Eq. (10), with the homogeneous white reflectivity assumption. On the satellite, for the hybrid DBF networks the SNR-preferred Type-A scanning beam-

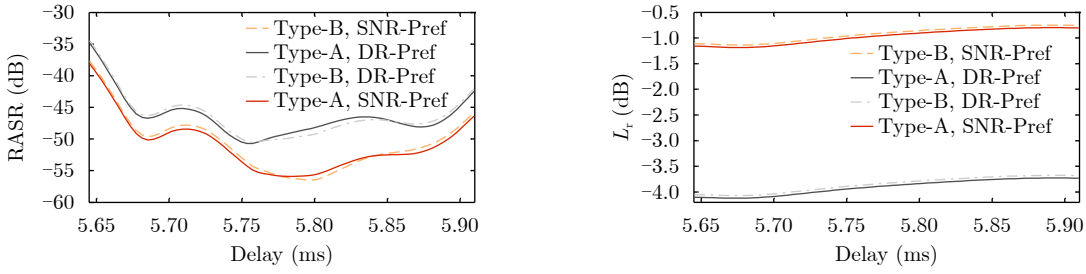

(a) RASR comparison (b) SNR comparison

Fig. 12 Across comparison of performance on RASR and SNR between the onboard transmit signal-structure-dependent beamformers (Type-B) and the non-signal-dependent ones (Type-A)

former, *i.e.* $\boldsymbol{w}_{\mathrm{DPSS}}(t)$ is employed as representative, with the deterministic DOA information calculated according to the default earth model (with a deviation of $\Delta h = 250$ m); For the onboard real-time null-steering DBF[7], the same deterministic mismatched DOA information is used. On the ground, for the hybrid DBF networks, the data-dependent adaptive beamformer presented in Section 3.3.2 is employed. In order to provide the reference theoretic optimum performance, a cascaded DBF networks employing ground quiescent beamforming using true topographic height information are also investigated.

The final performance of the data-dependent cascaded DBF networks at 32 evenly distributed positions across the swath are simulated and evaluated, the corresponding results are shown in Fig. 14 with diamond markers, in comparison with its theoretic performance curves, also with the performance curves calculated for the onboard ANS DBF[7]. It is found that under the DOA mismatch condition in the presence of topographic height error, the performance of onboard ANS DBF employing deterministic real-time beamformer degrade, especially in the aspect of range ambiguity suppression, an average RASR degradation as large as 23 dB is found. Nevertheless, by employing the hybrid DBF adding data-dependent a posteriori beamforming on the ground, although there are positions where observable degradations on RASR and SNR loss occur in contrast to the theoretic optimum performance under accurate DOA information, the full-swath performance as a whole does not deviate much.

6 Conclusions & Discussion

An important issue in a MWE-SAR system is the fulfillment of DBF on receive in elevation for a reliable separation of the mutually temporal overlapped echoes from multiple different transmit subpulses. In this paper, the performance of a separation approach employing hybrid DBF in elevation by combining the onboard real-time beamsteering and a posteriori DBF on the ground is elaborately investigated. From theoretical analysis and simulation, it is found that in comparison with the onboard real-time deterministic DBF[6,7], the employment of the hybrid DBF networks can avoid the "topographic height variation" problem under model mismatch conditions

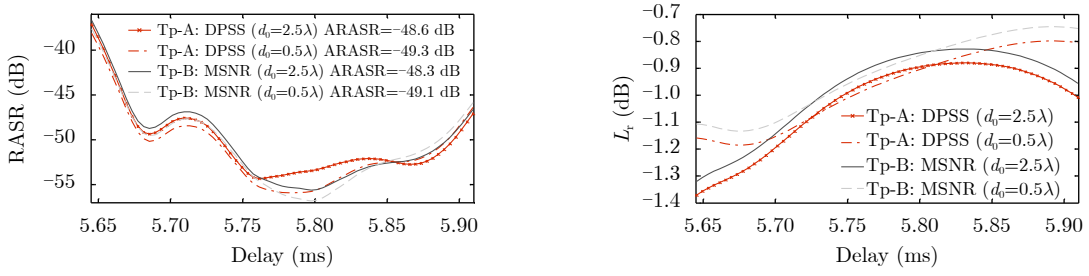

(a) RASR comparison (b) SNR comparison

Fig. 13 Performance on RASR and SNR for Type-A and Type-B SNR-preferred beamformers with an increased element spacing

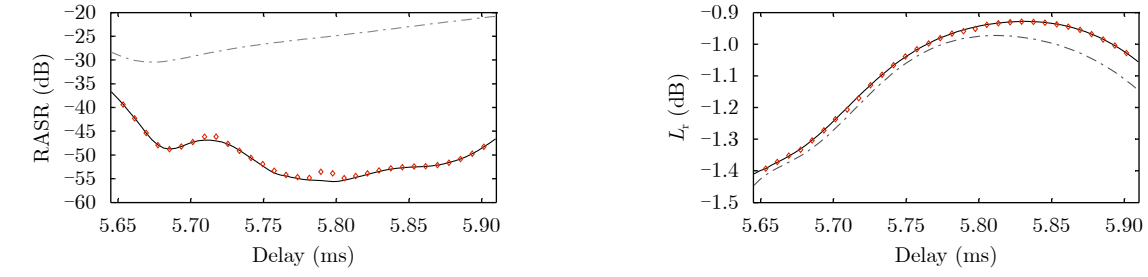

(a) RASR comparison (b) SNR comparison

Fig. 14 Performance on RASR and SNR of the cascaded DBF networks under the DOA mismatch condition in the presence of topographic height error, in comparison with the onboard real-time null-steering DBF in Ref. [7]

in the presence of topographic height variations, at the price of a small increase of the output data volume (in the present example, corresponding to the increase of the output channel number from 4 to 6). In comparison with the a posteriori DBF on the ground[8], employing the hybrid DBF networks can get similar (or even better) satisfactory performance while remarkably reducing the output data volume (in the present example, corresponding to the decrease of the output channel number from 10 to 6). It then can be concluded that the hybrid DBF approach can provide additional dimension of the trade-space to optimize the performance on SNR & RASR, as well as reduce onboard data volume.

It is also found that by making use of the transmit signal-structure information (Type-B networks), there indeed exists extra advantage with regard to the performance on SNR preserving, although this advantage may be rather limited in practical situations. It should be noted that due to the time-variant onboard beamforming, in either case of the Type-A or Type-B onboard DBF Networks, the signal distortion in range dimension exists. Although the distortion can be sufficiently avoidable by introducing additional constrains, a price of considerable signal gain loss has to be paid, for either the Type-A or Type-B Networks. Theoretically, the intra-subpulse distortion caused by the real-time PEL effect for Type-B DBF Networks is mitigated by introducing time delay and forming desired frequency dispersion. However, extra embedded real-time FIR filtering for each input data channel is essential, which will increase the onboard digital resources requirement.

$$\boldsymbol{A}^{(k)}(t)=\boldsymbol{\Lambda}(t)\boldsymbol{A}^{(k)}(\tau_{\mathrm{c}})\triangleq\boldsymbol{\Lambda}(t)\bar{\boldsymbol{A}}^{(k)} \tag{A-5}$$

$$\boldsymbol{\Lambda}(t)=\begin{bmatrix}1 & & & 0\\ & \mathrm{e}^{\mathrm{j}2\pi f_{\mathrm{c}}\left[\Delta\tau_m^{(k)}(t)-\Delta\tau_m^{(k)}(\tau_{\mathrm{c}})\right]} & \cdots & \\ 0 & & & \mathrm{e}^{\mathrm{j}2\pi(N-1)f_{\mathrm{c}}\left[\Delta\tau_m^{(k)}(t)-\Delta\tau_m^{(k)}(\tau_{\mathrm{c}})\right]}\end{bmatrix}$$

$$\approx\begin{bmatrix}1 & & & 0\\ & \mathrm{e}^{\mathrm{j}2\pi f_{\mathrm{b}}(t-\tau_{\mathrm{c}})} & \cdots & \\ 0 & & & \mathrm{e}^{\mathrm{j}2\pi(N-1)f_{\mathrm{b}}(t-\tau_{\mathrm{c}})}\end{bmatrix} \tag{A-6}$$

where

$$f_{\mathrm{b}}=\frac{d_0}{c}\times\left.\frac{\partial\sin\left[\beta(\tau)\right]}{\partial\tau}\right|_{\tau=\tau_{\mathrm{c}}}\times f_{\mathrm{c}} \tag{A-7}$$

It should be noted that in the expression following the squiggly equals sign in Eq. (A-6), we use the linear relationship between the off-boresight angle and echo delay at the swath center[6–8,22] implied in Eq. (A-7). It is pointed out in

Appendix A

After range compression on the ground, as derived in Ref. [8], $p_0(\xi)$ in Eq. (7) is replaced by the compressed version: $p_{\mathrm{comp}}(\xi)=\sqrt{P_{\mathrm{TB}}}\mathrm{sinc}(\pi K_{\mathrm{r}}T\xi)$ ($P_{\mathrm{TB}}=|K_{\mathrm{r}}|T_{\mathrm{p}}^2$ is the time-bandwidth product of the chirped subpulse), the pulse extent is compressed to only one range resolution bin $1/(K_{\mathrm{r}}T_{\mathrm{p}})$, so the approximation $\delta_{\Delta\tau_m^{(k)}}(\xi)\approx 0$ is valid and the following equation can be derived

$$\begin{aligned}s_{\mathrm{comp},m,ln}^{(k)}(t)&=\exp\left[\mathrm{j}2(lN+n)\pi f_{\mathrm{c}}\Delta\tau_m^{(k)}(t)\right]\times s_{\mathrm{comp},m}^{(k)}(t)\\&=\exp\left[\mathrm{j}2n\pi f_{\mathrm{c}}\Delta\tau_m^{(k)}(t)\right]\times s_{\mathrm{comp},m,l0}^{(k)}(t)\end{aligned} \tag{A-1}$$

where $s_{\mathrm{comp},m,ln}^{(k)}(t)$ and $s_{\mathrm{comp},m}^{(k)}(t)$ are the range compressed version of $s_{m,ln}^{(k)}(t)$ and $s_m^{(k)}(t)$, respectively. Then, the full form of the received signal vector $\boldsymbol{X}_{\mathrm{comp,sub\_}l}(t)$ comprising N-element echoes $x_{l0}(t),x_{l1}(t),\cdots,x_{l(N-1)}(t)$ within the subaperture l can be written in matrix form as[8]

$$\boldsymbol{X}_{\mathrm{comp,sub\_}l}(t)=\sum_{k=-\infty}^{\infty}\boldsymbol{A}^{(k)}(t)\boldsymbol{s}_{\mathrm{comp,sub\_}l}^{(k)}(t) \tag{A-2}$$

where $\boldsymbol{s}_{\mathrm{comp,sub\_}l}^{(k)}(t)=\left[s_{\mathrm{comp},-\frac{M-1}{2},l0}^{(k)},\cdots,s_{\mathrm{comp},m,l0}^{(k)},\cdots,s_{\mathrm{comp},\frac{M-1}{2},l0}^{(k)}\right]^{\mathrm{T}}$, which is comprised of echoes received by the reference element in each subaperture from the multiple transmit waveforms, $[\cdot]^{\mathrm{T}}$ denotes matrix transpose. $\boldsymbol{A}^{(k)}$ is the $N\times M$ steering matrix consisting of M subpulse-centred steering vectors

$$\boldsymbol{A}^{(k)}(t)=\left[\begin{array}{ccccc}\boldsymbol{a}_{-\frac{M-1}{2}}^{(k)}(t) & \cdots & \boldsymbol{a}_m^{(k)}(t) & \cdots & \boldsymbol{a}_{\frac{M-1}{2}}^{(k)}(t)\end{array}\right] \tag{A-3}$$

$$\boldsymbol{a}_m^{(k)}(t)=\left[\begin{array}{cccc}1 & \mathrm{e}^{\mathrm{j}2\pi f_{\mathrm{c}}\Delta\tau_m^{(k)}(t)} & \cdots & \mathrm{e}^{\mathrm{j}2\pi f_{\mathrm{c}}(N-1)\Delta\tau_m^{(k)}(t)}\end{array}\right]^{\mathrm{T}} \tag{A-4}$$

$\boldsymbol{A}^{(k)}(t)$ can be further expressed as

Ref. [5] that this approximation is effective for azimuth MWE SAR investigated in this paper, which is normally with a single swath. However, for elevation MWE SAR with multiple sub swaths discussed in ref.[5], this approximation may be invalid. In order to solve the multiple subswath problem, in Ref. [5] a spectrum-segment-based DSBF (digital scalloped beamforming) and adaptive multiple null-steering method is proposed. In this paper, for azimuth MWE SAR, we introduce two types of onboard digital beamformers (Type-A and Type-B) in the Section 3.2, and it will be found that Type-B beamformer will use the approximation in Eq. (A-7).

Appendix B

The generalized subaperture directivity defined on an angular extent rather than an angular point can be written as

$$D_{\psi_0}=\frac{\int_{-\psi_0}^{\psi_0}|B(\psi')|^2\mathrm{d}\psi'}{\int_{-\pi}^{\pi}|B(\psi')|^2\mathrm{d}\psi'}=\frac{\bar{\boldsymbol{w}}_{\mathrm{RT},\psi_c}^{\mathrm{H}}\boldsymbol{Q}_{\psi_0}\bar{\boldsymbol{w}}_{\mathrm{RT},\psi_c}}{\bar{\boldsymbol{w}}_{\mathrm{RT},\psi_c}^{\mathrm{H}}\boldsymbol{Q}_{\pi}\bar{\boldsymbol{w}}_{\mathrm{RT},\psi_c}} \tag{B-1}$$

It is found that maximizing the generalized subaperture directivity is equivalent to maximizing the proportion of the power pattern in the region $[-\psi_0,\psi_0]$ and the whole unambiguous region $[-\pi,\pi]$. Eq. (B-1) has a form of the generalized Rayleigh quotient. According to Rayleigh-Ritz theorem[28], the optimum $\bar{\boldsymbol{w}}_{\mathrm{RT}}$ that maximizes Eq. (B-1) is the eigenvector of the matrix $\boldsymbol{Q}_{\psi_0}$ corresponding to the maximum eigenvalue:

$$\begin{aligned}\bar{\boldsymbol{w}}_{\mathrm{RT}}&=\bar{\boldsymbol{w}}_{\mathrm{DPSS}}\\&=[\bar{w}_{\mathrm{DPSS},0},\bar{w}_{\mathrm{DPSS},1},\cdots,\bar{w}_{\mathrm{DPSS},L-1}]^{\mathrm{T}}\boldsymbol{I}_{\mathrm{s}}(-\psi_c)\end{aligned} \tag{B-2}$$

which fulfills $\sum_{l_1=0}^{N-1}\dfrac{\sin[(l_1-l_2)\psi_0]}{l_1-l_2}\bar{w}_{\mathrm{DPSS},l_1}=\pi\lambda\bar{w}_{\mathrm{DPSS},l_2}$, l_2=0, 1, ⋯, N–1, and classified as the first-order Discrete Prolate Spheroidal Serial (DPSS)[26].

Appendix C

Like what done in Appendix B, we can derive a weighting vector to relax the distortionless demand but prefer SNR performance. The optimization criteria is to maximize SNR under multi-component condition. According to the signal model Eq. (34), the SNR is given by

$$\left(\frac{S}{N}\right)_{\mathrm{sub}}=\frac{\boldsymbol{w}_{\mathrm{RT}}^{\mathrm{H}}(t)\boldsymbol{R}_{\boldsymbol{X}_{\mathrm{s}}}^{\mathrm{sub}}(t)\boldsymbol{w}_{\mathrm{RT}}(t)}{\sigma_{\mathrm{noise}}^2\boldsymbol{w}_{\mathrm{RT}}^{\mathrm{H}}(t)\boldsymbol{w}_{\mathrm{RT}}(t)} \tag{C-1}$$

$$\boldsymbol{R}_{\boldsymbol{X}_{\mathrm{s}}}^{\mathrm{sub}}(t)=\boldsymbol{A}^{(0)}(t)\boldsymbol{R}_{\mathrm{s}}^{\mathrm{sub}}(t)\boldsymbol{A}^{(0)\mathrm{H}}(t) \tag{C-2}$$

where $\boldsymbol{R}_{\mathrm{s}}^{\mathrm{sub}}(t)$ is the correlation matrix of the desired signal vector $\boldsymbol{s}_{\mathrm{sub}\_l}^{(0)}(t)$, which has a form of diagonal matrix as derived in detail in Appendix D. According to Rayleigh-Ritz theorem[28], the optimum $\boldsymbol{w}_{\mathrm{RT}}^{\mathrm{H}}(t)$ that maximizes Eq. (C-1) can be represented by

$$\boldsymbol{w}_{\mathrm{RT}}^{\mathrm{H}}(t)=\boldsymbol{w}_{\mathrm{MSNR}}^{\mathrm{H}}(t)=\boldsymbol{c}_{\max}^{\mathrm{H}}\boldsymbol{A}^{(0)\mathrm{H}}\approx\bar{\boldsymbol{w}}_{\mathrm{MSNR}}^{\mathrm{H}}\boldsymbol{\Lambda}^{\mathrm{H}}(t) \tag{C-3}$$

where $\boldsymbol{c}_{\max}^{\mathrm{H}}$ is the eigenvector of the matrix $\boldsymbol{R}_{\mathrm{s}}^{\mathrm{sub}}\left(\boldsymbol{A}^{(0)\mathrm{H}}\boldsymbol{A}^{(0)}\right)$ corresponding to the maximum eigenvalue, and $\bar{\boldsymbol{w}}_{\mathrm{MSNR}}^{\mathrm{H}}=\boldsymbol{w}_{\mathrm{MSNR}}^{\mathrm{H}}(\tau_c)$.

Appendix D

In this appendix, the cross-correlation of echoes from different subpulses/waveforms and PRIs is derived, for convenience, the reference-channel echo form is used. In order to give a general derivation, a general multi-transmit waveform scheme (cf. Eq. (3a)), rather than the specific time-shifted chirped subpulses, is used at the beginning. According to Eq. (4) and the definition of $g_m^{(k)}(\tau)$ in Ref. [8], the cross-correlation of $s_m^{(k)}(t)$ and $s_{m'}^{(k')}(t)$ received by the reference element can be expressed by

$$\begin{aligned}E[s_m^{(k)}(t)s_{m'}^{(k')*}(t)]&=\int_{-\infty}^{\infty}\int_{-\infty}^{\infty}E\left[g_m^{(k)}(t-\tau_1-kT_{\mathrm{r}})g_{m'}^{(k')*}(t-\tau_2-k'T_{\mathrm{r}})\right]p_m(\tau_1)\,p_{m'}^*(\tau_2)\,\mathrm{d}\tau_1\mathrm{d}\tau_2\\&=\delta(k'-k)\rho(m'-m,0)\,E_0\int_{-\infty}^{\infty}h^{(k)}(t-\tau)p_m(\tau)\,p_{m'}^*(\tau)\,\mathrm{d}\tau\end{aligned} \tag{D-1}$$

where

$$h^{(k)}(t)=\frac{|a_{\mathrm{T},m}(t-kT_{\mathrm{r}})|^2|a_{\mathrm{R},d_0}(t-kT_{\mathrm{r}})|^2}{(t-kT_{\mathrm{r}})^3\sin[\theta(t-kT_{\mathrm{r}})]} \tag{D-2}$$

is a slow-variant weighting function[11]which is dependent on the transmit and receive antenna pattern $a_{\mathrm{T},m}(\tau)$ and $a_{\mathrm{R},d_0}(\tau)$, round-trip delay $\tau=t-kT_{\mathrm{r}}$, and the incidence angel $\theta(\tau)$. E_0 is a

constant, and $\rho(m'-m, k'-k) \in [0, 1]$, describes the decorrelation caused by the variation of the illuminated patch with different transmit waveforms and PRIs. For the multi-beam mode concerned in this paper, $\rho(m'-m, k'-k) \approx 0$ if $m \neq m'$, since each subbeam covers its individual portion of the full illuminated azimuth footprint.

When $m \neq m'$, it is known from Ref. [11] that if the transmitted waveforms $p_m(\tau)$ and $p_{m'}(\tau)$ fulfill the short-term shift orthogonality condition, the integral value in the last row of Eq. (D-1) is equal to zero (cf. Eq. (4) and Eq. (7) in Ref. [8]). In particular, for the multi-beam mode employing the time-shifted subpulse scheme, both $\rho(m'-m, 0)$ and the integral value is zero, so it can be concluded that $E[s_m^{(k)}(t)s_{m'}^{(k')*}(t)] = 0$ if $m \neq m'$. When $m = m'$, $E[s_m^{(k)}(t)s_{m'}^{(k')*}(t)]$ can then be given by

$$E[s_m^{(k)}(t)s_m^{(k')*}(t)] = \delta(k'-k)E_0 \int_{-\infty}^{\infty} h^{(k)}(t-\tau) \cdot |p_m(\tau)|^2 \mathrm{d}\tau \triangleq \delta(k'-k)\sigma_m^{2(k)}(t) \tag{D-3}$$

If the linear time-shifted subpulse is used, $\sigma_m^{2(k)}(t)$ can be further evaluated by

$$\begin{aligned}\sigma_m^{2(k)}(t) &= E_0 \int_{-\frac{T_\mathrm{p}}{2}}^{\frac{T_\mathrm{p}}{2}} h^{(k)}(t-\xi-mT)\mathrm{d}\xi \\ &\approx E_0 T_\mathrm{p} h^{(k)}(t-mT)\end{aligned} \tag{D-4}$$

Note that the variation of $h^{(k)}(t)$ within a subpulse is ignored since it is a slow-variant weighting function.

In a very similar manner, the cross-correlation of echoes from different waveforms and different PRI after range focusing can also be given. If employing the time-shifted subpulse waveform scheme, the cross-correlation of range compressed $\tilde{s}_m^{(k)}(t)$ and $\tilde{s}_{m'}^{(k')}(t)$ can be expressed by

$$E[\tilde{s}_m^{(k)}(t)\tilde{s}_{m'}^{(k')*}(t)] = \delta(k'-k)\delta(m'-m)\tilde{\sigma}_m^{2(k)}(t) \tag{D-5}$$

where $\tilde{\sigma}_m^{2(k)}(t)$ can be approximately evaluated if the range match filter is an ideal passive power filter

$$\begin{aligned}\tilde{\sigma}_m^{2(k)}(t) &= E_0 P_\mathrm{TB} \int_{-\frac{T_\mathrm{p}}{2P_\mathrm{TB}}}^{\frac{T_\mathrm{p}}{2P_\mathrm{TB}}} h^{(k)}(t-mT-\xi)\mathrm{d}\xi \\ &\approx E_0 T_\mathrm{p} h^{(k)}(t-mT) = \sigma_m^{2(k)}(t)\end{aligned} \tag{D-6}$$

References

[1] MOREIRA A, PRATS-IRAOLA P, YOUNIS M, *et al*. A tutorial on synthetic aperture radar[J]. *IEEE Geoscience and Remote Sensing Magazine*, 2013, 1(1): 6–43. doi: 10.1109/MGRS.2013.2248301.

[2] KRIEGER G, GEBERT N, and MOREIRA A. Unambiguous SAR signal reconstruction from nonuniform displaced phase center sampling[J]. *IEEE Geoscience and Remote Sensing Letters*, 2004, 1(4): 260–264. doi: 10.1109/LGRS.2004.832700.

[3] GEBERT N, KRIEGER G, and MOREIRA A. Digital beamforming on receive: Techniques and optimization strategies for high-resolution wide-swath SAR imaging[J]. *IEEE Transactions on Aerospace and Electronic Systems*, 2009, 45(2): 564–592. doi: 10.1109/TAES.2009.5089542.

[4] KRIEGER G, GEBERT N, and MOREIRA A. Multidimensional waveform encoding: A new digital beamforming technique for synthetic aperture radar remote sensing[J]. *IEEE Transactions on Geoscience and Remote Sensing*, 2008, 46(1): 31–46. doi: 10.1109/TGRS.2007.905974.

[5] ZHAO Qingchao, ZHANG Yi, WANG Wei, *et al*. Echo separation for space-time waveform-encoding SAR with digital scalloped beamforming and adaptive multiple null-steering[J]. *IEEE Geoscience and Remote Sensing Letters*, 2020, in press. doi: 10.1109/LGRS.2020.2968811.

[6] FENG Fan, LI Shiqiang, YU Weidong, *et al*. Study on the processing scheme for space-time waveform encoding SAR system based on two-dimensional digital beamforming[J]. *IEEE Transactions on Geoscience and Remote Sensing*, 2012, 50(3): 910–932. doi: 10.1109/TGRS.2011.2162097.

[7] FENG Fan, LI Shiqiang, YU Weidong, *et al*. Echo separation in multidimensional waveform encoding SAR remote sensing using an advanced null-steering beamformer[J]. *IEEE Transactions on Geoscience and Remote Sensing*, 2012, 50(10): 4157–4172. doi: 10.1109/TGRS.2012.2187905.

[8] HE Feng, MA Xile, DONG Zhen, *et al*. Digital beamforming on receive in elevation for multidimensional waveform encoding SAR sensing[J]. *IEEE Geoscience and Remote Sensing Letters*, 2014, 11(12): 2173–2177. doi: 10.1109/LGRS.2014.2323267.

[9] 徐伟, 邓云凯. 基于多维编码信号星载MIMO-SAR的回波分离方法[J]. 电子科技大学学报, 2012, 41(1): 25–30. doi: 10.3969/j.issn.1001-0548.2012.01.005.
XU Wei and DENG Yunkai. Waveform diversity extraction in Spaceborne MIMO-SAR system based on multidimensional waveform encoding[J]. *Journal of University of Electronic Science and Technology of China*, 2012, 41(1): 25–30. doi: 10.3969/j.issn.1001-0548.2012.01.005.

[10] HE Feng, DONG Zhen, and LIANG Diannong. A novel space-time coding Alamouti waveform scheme for MIMO-

SAR[J]. *IEEE Geoscience and Remote Sensing Letters*, 2015, 12(2): 229–233. doi: 10.1109/LGRS.2014.2333232.

[11] KRIEGER G. MIMO-SAR: Opportunities and pitfalls[J]. *IEEE Transactions on Geoscience and Remote Sensing*, 2014, 52(5): 2628–2645. doi: 10.1109/TGRS.2013.2263934.

[12] YOUNIS M, KRIEGER G, and MOREIRA A. MIMO SAR techniques and trades[C]. 2013 IEEE European Radar Conference, Nuremberg, Germany, 2013: 141–144.

[13] DIEBOLD A V, IMANI M F, and SMITH D R. Phaseless radar coincidence imaging with a MIMO SAR platform[J]. *Remote Sensing*, 2019, 11(5): 533. doi: 10.3390/rs11050533.

[14] HUANG Pingping and XU Wei. ASTC-MIMO-TOPS mode with digital beam-forming in elevation for high-resolution wide-swath imaging[J]. *Remote Sensing*, 2015, 7(3): 2952–2970. doi: 10.3390/rs70302952.

[15] KIM J, YOUNIS M, MOREIRA A, *et al*. Spaceborne MIMO synthetic aperture radar for multimodal operation[J]. *IEEE Transactions on Geoscience and Remote Sensing*, 2015, 53(5): 2453–2466. doi: 10.1109/TGRS.2014.2360148.

[16] WANG Wenqin. MIMO SAR imaging: Potential and challenges[J]. *IEEE Aerospace and Electronic Systems Magazine*, 2013, 28(8): 18–23. doi: 10.1109/MAES.2013.6575407.

[17] WANG Jie, LIANG Xingdong, DING Chibiao, *et al*. A novel scheme for ambiguous energy suppression in MIMO-SAR systems[J]. *IEEE Geoscience and Remote Sensing Letters*, 2015, 12(2): 344–348. doi: 10.1109/LGRS.2014.2340898.

[18] QI Weikong and YU Weidong. A novel operation mode for spaceborne polarimetric SAR[J]. *Science China Information Sciences*, 2011, 54(4): 884–897. doi: 10.1007/s11432-011-4183-1.

[19] YOUNIS M, HUBER S, PATYUCHENKO A, *et al*. Performance comparison of reflector- and planar-antenna based digital beam-forming SAR[J]. *International Journal of Antennas and Propagation*, 2009, 2009: 614931.

[20] ZHAO Qingchao, ZHANG Yi, WANG Wei, *et al*. On the frequency dispersion in DBF SAR and digital scalloped beamforming[J]. *IEEE Transactions on Geoscience and Remote Sensing*, 2020, 58(5): 3619–3632. doi: 10.1109/TGRS.2019.2958863.

[21] YOUNIS M, ROMMEL T, BORDONI F, *et al*. On the pulse extension loss in digital beamforming SAR[J]. *IEEE Geoscience and Remote Sensing Letters*, 2015, 12(7): 1436–1440. doi: 10.1109/LGRS.2015.2406815.

[22] SUESS M and WIESBECK W. Side-looking synthetic aperture radar system[J]. *European Patent EP*, 2002, 1(241): 487.

[23] BORDONI F, YOUNIS M, VARONA E M, *et al*. Performance investigation on scan-on-receive and adaptive digital beam-forming for high-resolution wide-swath synthetic aperture radar[C]. International ITG Workshop of Smart Antennas, Berlin, Germany, 2009: 114–121.

[24] WANG Wei, WANG R, DENG Yunkai, *et al*. An improved processing scheme of digital beam-forming in elevation for reducing resource occupation[J]. *IEEE Geoscience and Remote Sensing Letters*, 2016, 13(3): 309–313.

[25] OPPENHEIM A V, SCHAFER R W, and BUCK J R. Discrete-Time Signal Processing[M]. 2nd ed. Upper Saddle River: Prentice-Hall, 1999.

[26] VAN TREES H L. Optimum Array Processing: Part IV of Detection, Estimation, and Modulation Theory[M]. New York, USA: Wiley-Interscience Press, 2002.

[27] GUERCI J R. Theory and application of covariance matrix tapers for robust adaptive beamforming[J]. *IEEE Transactions on Signal Processing*, 1999, 47(4): 977–985. doi: 10.1109/78.752596.

[28] GOLUB G H and VAN LOAN C F. Matrix Computations[M]. 2nd ed. Baltimore: The Johns Hopkins University Press, 1989.

HE Feng received the B.S. and Ph.D. degrees in signal processing from National University of Defense Technology, Changsha, in 1998 and 2005, respectively. From March 2015 to September 2015, he joined the scientific staff of the Technical University of Munich to work within a cooperation framework at the Microwaves and Radar Institute, German Aerospace Center (DLR), Wessling, Germany. Here as a visiting scholar, he participated in the distributed spaceborne SAR research work. He is currently a professor with the College of Electronic Science and Technology, National University of Defense Technology. His current major research interests include SAR processing, array processing, and MIMO radar system.

E-mail: hefeng@nudt.edu.cn

ZHANG Yongsheng was born in Inner Mongolia, China, in December 1977. He received the Ph.D. degrees in electronics and information engineering from National University of Defense Technology in 2007. He is currently a professor with the College of Electronic Science and Technology, National University of Defense Technology. His current major research interests include SAR system design and SAR data processing.

E-mail: zhangyongsheng@nudt.edu.cn

SUN Zaoyu was born in Hubei, China, in July 1978. He received the B.S. and Ph.D. degrees in signal processing from National University of Defense Technology, Changsha, in 2000 and 2008, respectively. He is currently a lecturer with the College of Electronic Science and Technology, National University of Defense Technology. His research interests include SAR and InSAR processing.

E-mail: sunzaoyu@nudt.edu.cn

JIN Guanghu was born in Anhui, China, in February 1980. He received the B.E., M.S. and Ph.D. degrees in signal processing from National University of Defense Technology, Changsha, in 2002, 2004 and 2009 respectively. He is currently an associate professor with the College of Electronic Science and Technology, National University of Defense Technology. His research interests include Synthetic Aperture Radar (SAR), inverse SAR, and radar target recognition.

E-mail: guanghujin@nudt.edu.cn

DONG Zhen was born in Anhui, China, in September 1973. He received the Ph.D. degree in electrical engineering from National University of Defense Technology, Changsha in 2001. He is currently a professor with the College of Electronic Science and Technology, National University of Defense Technology. His recent research interests include SAR system design and processing, Ground Moving Target Indication (GMTI), and digital beamforming.

E-mail: dongzhen@nudt.edu.cn